

The Moving Discontinuous Galerkin Method with Interface Condition Enforcement for Robust Simulations of High-Speed Viscous Flows

Eric J. Ching, Andrew D. Kercher, Andrew Corrigan

Laboratories for Computational Physics and Fluid Dynamics, U.S. Naval Research Laboratory, 4555 Overlook Ave SW, Washington, DC 20375

Abstract

The moving discontinuous Galerkin method with interface condition enforcement (MDG-ICE) is a high-order, r -adaptive method that treats the grid as a variable and weakly enforces the conservation law, constitutive law, and corresponding interface conditions in order to implicitly fit high-gradient flow features. In this paper, we introduce nonlinear solver strategies to more robustly and efficiently compute high-speed viscous flows. Specifically, we incorporate an anisotropic grid regularization based on the mesh-implied metric into the nonlinear least-squares solver that inhibits grid motion in directions with small element length scales. Furthermore, we develop an adaptive elementwise regularization strategy that locally scales the regularization terms as needed to maintain grid validity. We apply the proposed MDG-ICE formulation to test cases involving viscous shocks and/or boundary layers, including Mach 17.6 hypersonic viscous flow over a circular cylinder and Mach 5 hypersonic viscous flow over a sphere, which are very challenging test cases for conventional numerical schemes on simplicial grids. Even without artificial dissipation, the computed solutions are free from spurious oscillations and yield highly symmetric surface heat-flux profiles.

Keywords: High-order method; Discontinuous Galerkin method; Interface condition enforcement; MDG-ICE; Implicit shock fitting; Anisotropic curvilinear r -adaptivity; Mesh adaptation

1. Introduction

The moving discontinuous Galerkin finite element method with interface condition enforcement (MDG-ICE) is an implicit shock fitting method capable of handling complex shock dynamics [1, 2, 3]. The method is a unique variation of the well-known discontinuous Galerkin (DG) method [4, 5]. Specifically, neighboring elements are not coupled through interfacial, single-valued numerical fluxes; instead, the conservation law and interface conditions (known as the generalized Rankine-Hugoniot jump conditions [6]) are directly discretized, and the grid is treated as a variable. By simultaneously solving for the flow field and discrete geometry, MDG-ICE is able to produce extremely accurate solutions on coarse grids *without artificial dissipation* as the grid points are automatically adjusted to fit shocks and resolve smooth regions of the flow with sharp gradients. This has significant advantages over traditional shock capturing approaches, such as artificial viscosity and limiting; the former can significantly smear discontinuous and high-gradient features (and even cause movement of such features that may then contaminate prediction of other flow structures [7]) and introduce low-order errors into nominally high-order approximations, while the latter can obstruct iterative convergence, fail to provide sufficient stabilization, and be used only for certain polynomial degrees and/or element types. Furthermore, since MDG-ICE adapts the grid to satisfy the weak form, grid interfaces are naturally repositioned to fit a priori unknown shocks with arbitrary topology, overcoming key limitations

of explicit shock fitting methods. Note that in the inviscid case, shocks are fit exactly along grid interfaces, while in the viscous setting, high-aspect-ratio cells form to resolve viscous shocks, which are sharp (yet smooth) features, via anisotropic curvilinear r -adaptivity. In previous work, MDG-ICE was shown to achieve not only extremely sharp, oscillation-free viscous-shock profiles, but also superior convergence rates and significantly higher accuracy than standard DG schemes in boundary-layer problems [2]. Another form of implicit shock fitting is the high-order implicit shock tracking (HOIST) framework developed by Zahr and Persson [8] and improved in [9, 10, 11, 12], which also treats the discrete geometry as a variable while retaining a standard discontinuous Galerkin method. High-quality solutions to inviscid flows with discontinuities on coarse grids have been achieved using HOIST. Additionally, a variant of MDG-ICE has been developed by Luo et al. [13].

Figure 1.1 presents representative results for hypersonic viscous flow over a half-cylinder at Mach 5 and Reynolds number 10^4 on a triangular grid. A $\text{DG}(\mathcal{P}_1)$ solution (where \mathcal{P}_p denotes the space of polynomials of total degree p on simplicial elements) with artificial viscosity is compared with the $\text{MDG-ICE}(\mathcal{P}_4)$ solution without any additional stabilization. Unlike in the MDG-ICE solution, the shock in the DG solution is noticeably smeared, and spurious oscillations are visible both at the shock and in the shock layer. The resulting surface heating profile in the MDG-ICE solution is highly symmetric, which, despite the relatively simple flow conditions, is nevertheless encouraging since surface heat-flux predictions in state-of-the-practice finite-volume simulations of external hypersonic flows are known to deteriorate considerably when using simplicial grids [14, 15]. In particular, finite-volume schemes are extremely sensitive to misalignment between the grid and the shock and boundary layer, which generates errors in vorticity and entropy that propagate downstream and pollute surface quantities. Shock-tailored quadrilateral/hexahedral grids are typically needed to obtain heat-flux profiles that do not exhibit noticeable nonphysical asymmetries. Constructing such grids for large-scale geometries often requires significant time and user effort, which is exacerbated when performing parametric studies.

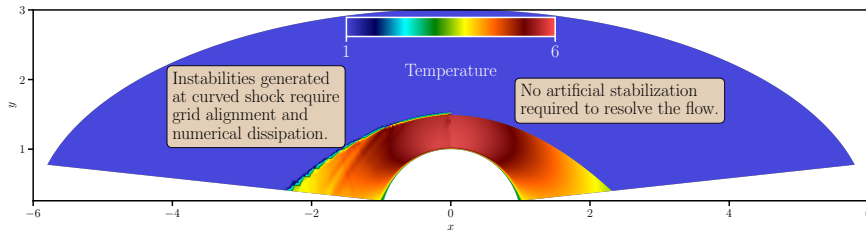


Figure 1.1: Comparison of the $\text{DG}(\mathcal{P}_1)$ (with artificial viscosity) (left) and $\text{MDG-ICE}(\mathcal{P}_4)$ (right) solutions to the viscous Mach 5 bow shock at $\text{Re} = 10^4$ [2].

However, a major difficulty encountered in MDG-ICE calculations is frequent cell degeneration (i.e., the determinant of the geometric Jacobian becomes negative), particularly as curved, high-aspect-ratio cells form to resolve sharp viscous features. Figure 1.2 displays the final mesh for an MDG-ICE solution to the same cylinder problem, but with a higher Reynolds number [2]. Degenerate cells were treated via longest-edge refinement, leading to the generation of “sliver” elements that introduce unnecessary degrees of freedom. Furthermore, although adequate for this relatively simple flow, in problems of moderately greater complexity, this strategy either requires an inordinate number of refinements or, worse, simply fails to recover a valid grid. Given this significant bottleneck precluding the application of MDG-ICE to more complicated, larger-scale configurations, the primary objective of this work is to equip MDG-ICE with enhanced solver strategies to enable robust and accurate computations of hypersonic viscous flows in two and three dimensions without artificial dissipation. First, we leverage the mesh-implied metric, which encodes information about the local element size and orientation (even on curved, anisotropic grids) [16]. In particular, we incorporate the metric into the Levenberg-Marquardt nonlinear least-squares solver through an anisotropic grid regularization that inhibits grid motion in directions with small element length scales. This is similar to the inverse-volume scaling introduced by Zahr et al. [9] and employed in [3], but with element anisotropy explicitly taken into account. Furthermore, we incorporate additional regularization operators and develop an adaptive

elementwise regularization procedure that locally increases regularization parameters as needed to maintain grid validity. We also employ increment limiting as described in [17], where the increment at each iteration is dynamically reduced to mitigate excessive changes in pressure and/or density. These solver strategies, combined with a full parallelization of our MDG-ICE implementation, enable consideration of much more challenging hypersonic test cases. We specifically employ simplicial grids that are initially coarse with respect to the final high-gradient features in order to demonstrate the potential of MDG-ICE to significantly alleviate the burden of mesh generation on the user. Finally, we note that although incorporating artificial dissipation into the formulation in some capacity (e.g., applied only during intermediate iterations or minimally in the final solution) may be beneficial, the present study aims to aggressively test the underlying MDG-ICE formulation without the aid of additional stabilization and, as a secondary goal, identify where stabilization would be most useful; incorporation of such dissipation mechanisms is left for future work.

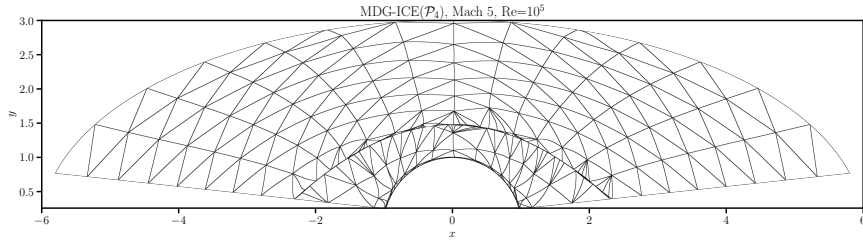


Figure 1.2: Final mesh for MDG-ICE solution to viscous Mach 5 bow shock at $\text{Re} = 10^5$ [2].

The remainder of this paper is organized as follows. Sections 2 and 3 briefly summarize the governing equations considered in this study and the basic MDG-ICE formulation, respectively. The enhanced nonlinear solver is then detailed in Section 4. The following section presents results for a variety of challenging test cases, including two- and three-dimensional hypersonic viscous flows over blunt bodies in which surface heat flux is a target quantity. We conclude with final remarks and recommendations for future work.

2. Governing equations

Consider the following nonlinear conservation law:

$$\nabla \cdot \mathcal{F}(y, \nabla_x y) = 0 \text{ in } \Omega, \quad (2.1)$$

where y is the state variable, \mathcal{F} is the flux, $\nabla_x(\cdot)$ denotes the spatial gradient, and Ω is the domain. In the case of a space-time domain of dimension d , the space-time flux is given by

$$\mathcal{F}(y, \nabla_x y) = (\mathcal{F}_1^x(y, \nabla_x y), \dots, \mathcal{F}_{d_x}^x(y, \nabla_x y), y), \quad (2.2)$$

where $d_x = d - 1$ is the number of spatial dimensions and $\mathcal{F}^x(y, \nabla_x y) = \mathcal{F}^c(y) - \mathcal{F}^v(y, \nabla_x y)$ is the spatial flux, consisting of both the convective flux, $\mathcal{F}^c(y)$, and the viscous flux, $\mathcal{F}^v(y)$. The divergence operator in Equation (2.1) is then the space-time divergence operator, given by

$$\nabla \cdot \mathcal{F}(y, \nabla_x y) = \nabla_x \cdot \mathcal{F}^x(y, \nabla_x y) + \frac{\partial}{\partial t} y. \quad (2.3)$$

In the case of a spatial domain, the flux is simply the spatial flux, and the divergence operator is the spatial divergence operator. In this study, we consider the viscous Burgers equation and the compressible Navier-Stokes equations.

2.1. One-dimensional viscous Burgers equation

For the one-dimensional viscous Burgers equation, the convective and viscous fluxes are given by

$$\mathcal{F}^c(y) = \left(\frac{1}{2} y^2 \right), \quad \mathcal{F}^v(y, \nabla_x y) = \mu \nabla_x y, \quad (2.4)$$

where μ is the viscosity. The spatial flux is then written as

$$\mathcal{F}^x(y, \nabla_x y) = \left(\frac{1}{2} y^2 - \mu \nabla_x y \right), \quad (2.5)$$

2.2. Compressible Navier-Stokes equations

The vector of state variables is given by

$$y = (\rho, \rho v_1, \dots, \rho v_{d_x}, \rho E), \quad (2.6)$$

where ρ is the density, $v = (v_1, \dots, v_{d_x})$ is the velocity vector, and E is the specific total energy. The i th spatial component of the convective flux is

$$\mathcal{F}_i^c(y) = (\rho v_i, \rho v_i v_1 + P \delta_{i1}, \dots, \rho v_i v_{d_x} + P \delta_{id_x}, \rho H v_i), \quad (2.7)$$

where P is the pressure, δ_{ij} is the Kronecker delta, and $H = (\rho E + P) / \rho$ is the specific total enthalpy. In this work, we assume a calorically perfect gas, such that

$$P = (\gamma - 1) \left(\rho E - \frac{1}{2} \sum_{i=1}^{d_x} \rho v_i v_i \right), \quad (2.8)$$

where γ is the specific heat ratio, set to 1.4.

The i th spatial component of the viscous flux is

$$\mathcal{F}_i^\nu(y, \nabla_x y) = \left(0, \tau_{1i}, \dots, \tau_{d_x i}, \sum_{j=1}^{d_x} \tau_{ij} v_j - q_i \right), \quad (2.9)$$

where q is the heat flux and τ is the viscous stress tensor. The heat flux is expanded as $q = -\kappa \nabla_x T$, where κ is the thermal conductivity and T is the temperature, calculated as $T = P / (\rho R)$, with $R = 287$ denoting the specific gas constant. The i th spatial component of the viscous stress tensor is given by

$$\tau_i = \mu \left(\frac{\partial v_1}{\partial x_i} + \frac{\partial v_i}{\partial x_1} - \delta_{i1} \frac{2}{3} \sum_{j=1}^{d_x} \frac{\partial v_j}{\partial x_j}, \dots, \frac{\partial v_{d_x}}{\partial x_i} + \frac{\partial v_i}{\partial x_{d_x}} - \delta_{id_x} \frac{2}{3} \sum_{j=1}^{d_x} \frac{\partial v_j}{\partial x_j} \right), \quad (2.10)$$

where μ is the dynamic viscosity given by Sutherland's law. The thermal conductivity is computed using the constant-Prandtl-number assumption, $\text{Pr} = 0.72$.

Two important nondimensional quantities that characterize compressible, viscous flows are the Reynolds number, Re , and Mach number, Ma , defined as

$$\text{Re} = \frac{\rho |v| L}{\mu}, \quad (2.11)$$

where L is a characteristic length scale, and

$$\text{Ma} = \frac{|v|}{c}, \quad (2.12)$$

where $c = \sqrt{\gamma P / \rho}$ is the speed of sound, respectively.

3. Moving discontinuous Galerkin method with interface condition enforcement

In this subsection, we briefly review the MDG-ICE formulation for compressible, viscous flows. Further details can be found in [2], and an alternative least-squares formulation is described in [3].

Let Ω be partitioned by \mathcal{T} , which consists of cells κ . Furthermore, we define the set \mathcal{E} of interfaces such that $\bigcup_{\epsilon \in \mathcal{E}} = \bigcup_{\kappa \in \mathcal{T}} \partial \kappa$. The normal over each interface $\epsilon \in \mathcal{E}$ is denoted n . For space-time domains, n_x denotes the spatial normal.

3.1. Strong and weak formulations

Consider the following conservation law, constitutive law, and associated interface conditions in strong form:

$$\nabla \cdot \mathcal{F}(y, \sigma) = 0 \text{ in } \kappa \quad \forall \kappa \in \mathcal{T}, \quad (3.1)$$

$$\sigma - G(y) \nabla_x y = 0 \text{ in } \kappa \quad \forall \kappa \in \mathcal{T}, \quad (3.2)$$

$$\llbracket n \cdot \mathcal{F}(y, \sigma) \rrbracket = 0 \text{ on } \epsilon \quad \forall \epsilon \in \mathcal{E}, \quad (3.3)$$

$$\llbracket G(y) \rrbracket \llbracket y \otimes n_x \rrbracket = 0 \text{ on } \epsilon \quad \forall \epsilon \in \mathcal{E}, \quad (3.4)$$

where σ is an auxiliary variable, $G(y)$ is the homogeneity tensor that satisfies $G(y) \nabla_x y = \mathcal{F}^v(y, \nabla_x y) = \mathcal{F}_{\nabla_x y}^v(y, \nabla_x y) \nabla_x y$ (assuming the viscous flux is linear with respect to the spatial gradient of the state), and $\{\cdot\}$ and $\llbracket \cdot \rrbracket$ denote the average and jump operators, respectively. The interface condition (3.3), which corresponds to the conservation law (3.1), is known as the jump or generalized Rankine-Hugoniot conditions [6]. The interface condition (3.4), derived in [2], is associated with the constitutive law (3.2) and constrains the continuity of the state variable at the interface.

Let the solution spaces Y and Σ be the broken Sobolev spaces

$$Y = \left\{ y \in [L^2(\Omega)]^m \mid \forall \kappa \in \mathcal{T}, \quad y|_{\kappa} \in [H^1(\kappa)]^m \right\}, \quad (3.5)$$

$$\Sigma = \left\{ \sigma \in [L^2(\Omega)]^{m \times d_x} \mid \forall \kappa \in \mathcal{T}, \quad \nabla_x \cdot \sigma|_{\kappa} \in [L^2(\Omega)]^m \right\}. \quad (3.6)$$

The MDG-ICE weak formulation is then obtained by integrating Equations (3.1)-(3.4) against separate test functions: find $(y, \sigma) \in Y \times \Sigma$ such that

$$\begin{aligned} 0 = & \sum_{\kappa \in \mathcal{T}} (\nabla \cdot \mathcal{F}(y, \sigma), v_y)_{\kappa} \\ & + \sum_{\kappa \in \mathcal{T}} (\sigma - G(y) \nabla_x y, v_{\sigma})_{\kappa} \\ & - \sum_{\epsilon \in \mathcal{E}} (\llbracket n \cdot \mathcal{F}(y, \sigma) \rrbracket, w_y)_{\epsilon} \\ & - \sum_{\epsilon \in \mathcal{E}} (\llbracket G(y) \rrbracket \llbracket y \otimes n_x \rrbracket, w_{\sigma})_{\epsilon} \quad \forall (v_y, v_{\sigma}, w_y, w_{\sigma}) \in V_y \times V_{\sigma} \times W_y \times W_{\sigma}. \end{aligned} \quad (3.7)$$

where the test spaces are $V_y = [L^2(\Omega)]^m$ and $V_{\sigma} = [L^2(\Omega)]^{m \times d}$, with W_y and W_{σ} defined as the corresponding single-valued trace spaces. Note that numerical flux functions are not employed in the MDG-ICE formulation.

To treat the grid as a variable, the weak formulation (3.7) is transformed from physical to reference space. Let $u : \hat{\Omega} \rightarrow \Omega$ be a continuous, invertible mapping from the reference domain, $\hat{\Omega}$, to the physical domain, Ω . $\hat{\Omega}$ is assumed to be partitioned by $\hat{\mathcal{T}}$, such that $\hat{\Omega} = \cup_{\hat{\kappa} \in \hat{\mathcal{T}}} \hat{\kappa}$. Furthermore, let $\hat{\mathcal{E}}$ denote the set of interfaces, $\hat{\epsilon}$, such that $\cup_{\hat{\epsilon} \in \hat{\mathcal{E}}} \hat{\epsilon} = \cup_{\hat{\kappa} \in \hat{\mathcal{T}}} \partial \hat{\kappa}$. The solution and test spaces are also now assumed to be defined over reference space. We then define a provisional state operator, $\tilde{e} : Y \times \Sigma \times U \rightarrow (V_y \times V_{\sigma} \times W_y \times W_{\sigma})^*$ for $(y, \sigma, u) \in Y \times \Sigma \times U$, as

$$\begin{aligned} \tilde{e}(y, \sigma, u) = (v_y, v_{\sigma}, w_y, w_{\sigma}) \mapsto & \sum_{\hat{\kappa} \in \hat{\mathcal{T}}} ((\text{cof}(\nabla u) \nabla) \cdot \mathcal{F}(y, \sigma), v_y)_{\hat{\kappa}} \\ & + \sum_{\hat{\kappa} \in \hat{\mathcal{T}}} (\det(\nabla u) \sigma - G(y) (\text{cof}(\nabla u) \nabla)_x y, v_{\sigma})_{\hat{\kappa}} \\ & - \sum_{\hat{\epsilon} \in \hat{\mathcal{E}}} (\llbracket s(\nabla u) \cdot \mathcal{F}(y, \sigma) \rrbracket, w_y)_{\hat{\epsilon}} \\ & - \sum_{\hat{\epsilon} \in \hat{\mathcal{E}}} (\llbracket G(y) \rrbracket \llbracket y \otimes s(\nabla u)_x \rrbracket, w_{\sigma})_{\hat{\epsilon}}. \end{aligned} \quad (3.8)$$

The state operator, $e : Y \times \Sigma \times U \rightarrow (V_y \times V_\sigma \times W_y \times W_\sigma)^*$, is defined as

$$e(y, \sigma, u) = \tilde{e}(y, \sigma, b(u)), \quad (3.9)$$

which imposes geometric boundary conditions via the geometric projection operator, $b(u)$.

The state equation in reference space is $e(y, \sigma, u) = 0$, such that the corresponding weak formulation in reference space is as follows: find $(y, \sigma, u) \in Y \times \Sigma \times U$ such that

$$\langle e(y, \sigma, u), (v_y, v_\sigma, w_y, w_\sigma) \rangle = 0 \quad \forall (v_y, v_\sigma, w_y, w_\sigma) \in V_y \times V_\sigma \times W_y \times W_\sigma. \quad (3.10)$$

The solution is therefore given by $(y, \sigma, b(u)) \in Y \times \Sigma \times U$.

3.2. Discretization

To discretize the weak formulation (3.10), we choose discrete subspaces $Y_h \subset Y$, $\Sigma_h \subset \Sigma$, $U_h \subset U$, $V_{y,h} \subset V_y$, $V_{\sigma,h} \subset V_\sigma$, $W_{y,h} \subset W_y$, and $W_{\sigma,h} \subset W_\sigma$ and define a discrete state operator

$$e_h : Y_h \times \Sigma_h \times U_h \rightarrow \mathbb{R}^{\dim(V_{y,h} \times V_{\sigma,h} \times W_{y,h} \times W_{\sigma,h})}. \quad (3.11)$$

For a simplicial grid,

$$Y_h = \left\{ y \in Y \mid \forall \hat{\kappa} \in \hat{\mathcal{T}}, y|_{\hat{\kappa}} \in [\mathcal{P}_p]^m \right\}, \quad (3.12)$$

$$\Sigma_h = \left\{ \sigma \in \Sigma \mid \forall \hat{\kappa} \in \hat{\mathcal{T}}, \sigma|_{\hat{\kappa}} \in [\mathcal{P}_p]^{m \times d_x} \right\}, \quad (3.13)$$

where \mathcal{P}_p is the space of polynomials spanned by the monomials \mathbf{x}^β with multi-index $\beta \in \mathbb{N}_0^d$ satisfying $\sum_{i=1}^d \beta_i \leq p$. We set $V_{y,h} = Y_h$ and $V_{\sigma,h} = \Sigma_h$. $W_{y,h}$ and $W_{\sigma,h}$ are selected to be the corresponding single-valued polynomial trace spaces. The discrete subspace U_h of geometric mappings is defined as

$$U_h = \left\{ u \in U \mid \forall \hat{\kappa} \in \hat{\mathcal{T}}, u|_{\hat{\kappa}} \in [\mathcal{P}_p]^d \right\}. \quad (3.14)$$

In this work, the polynomial degrees of Y_h and Σ_h are chosen to be equal; the polynomial degree of U_h , however, may be different. The cases in which the polynomial degree of U_h is greater than, the same as, and less than the polynomial degrees of Y_h and Σ_h are referred to as superparametric, isoparametric, and subparametric, respectively.

4. Nonlinear solver

The weak formulation is solved iteratively (in nondimensional form) using unconstrained optimization to minimize the objective function

$$J(y, \sigma, u) = \frac{1}{2} \|e_h(y, \sigma, u)\|^2 \quad (4.1)$$

by seeking a stationary point

$$\nabla J(y, \sigma, u) = e_h'(y, \sigma, u)^* e_h(y, \sigma, u) = 0, \quad (4.2)$$

where $e_h'(y, \sigma, u)^* : \mathbb{R}^{\dim(V_{y,h} \times V_{\sigma,h} \times W_{y,h} \times W_{\sigma,h})} \rightarrow Y_h \times \Sigma_h \times U_h$ is the adjoint operator. Given an initialization $(y, \sigma, u)_0$, the solution is repeatedly updated

$$(y, \sigma, u)_{i+1} = (y, \sigma, u)_i + \Delta(y, \sigma, u)_i \quad i = 0, 1, 2, \dots \quad (4.3)$$

until (4.2) is satisfied to a given tolerance. We employ a Levenberg-Marquardt method [18, 19] to solve (4.2), which yields the increment

$$\Delta(y, \sigma, u) = - \left(e_h'(y, \sigma, u)^* e_h'(y, \sigma, u) + I_\lambda(y, \sigma, u) \right)^{-1} \left(e_h'(y, \sigma, u)^* e_h(y, \sigma, u) \right), \quad (4.4)$$

where the regularization operator is given by

$$I_\lambda(y, \sigma, u) : (\delta y, \delta \sigma, \delta u) \mapsto (\lambda_y \delta y, \lambda_\sigma \delta \sigma, \lambda_u \delta u), \quad (4.5)$$

with λ_y , λ_σ , and λ_u denoting the regularization coefficients. In practice, λ_y and λ_σ are set to zero. In addition to the identity regularization (4.5), which ensures positive definiteness and prevents large-scale grid changes, we incorporate a Laplacian-type grid regularization,

$$I_\lambda^\Delta : \delta u \mapsto (\nabla(b'_h(u)\delta u), \lambda_{\Delta u} \nabla(b'_h(u)v_u)), \quad (4.6)$$

where $\lambda_{\Delta u} \geq 0$ is the corresponding regularization coefficient and $v_u \in U_h$, which introduces a compressibility effect into the grid motion. In previous work [3], following the approach of Zahr et al. [9], the regularization factor $\lambda_{\Delta u}$ was modified to incorporate a factor proportional to the inverse of the element volume, which locally stiffens small elements in an *isotropic* manner. Note that the regularizations (4.5) and (4.6) are not incorporated into the objective function (4.1).

The solver as hitherto described was employed in [2]. In the remainder of this section, we introduce enhancements to the solver that significantly improve its robustness.

4.1. Additional regularization terms

4.1.1. Anisotropic Laplacian-type grid regularization

In this work, we modify the regularization (4.6) to directly account for element anisotropy as

$$I_\lambda^\Delta : \delta u \mapsto (\nabla(\mathcal{H}^{-\alpha} b'_h(u)\delta u), \lambda_{\Delta u} \nabla(b'_h(u)v_u)), \quad (4.7)$$

where $\alpha \geq 0$ is a parameter and \mathcal{H} , in the two-dimensional case, is an element-local, 2×2 , symmetric-positive-definite transformation matrix given by [16, 20]

$$\mathcal{H} = \mathcal{M}^{-1/2} = V \Sigma V^T = \begin{bmatrix} | & | \\ \hat{e}_1 & \hat{e}_2 \\ | & | \end{bmatrix} \begin{bmatrix} h_1 & 0 \\ 0 & h_2 \end{bmatrix} \begin{bmatrix} - & \hat{e}_1^T & - \\ - & \hat{e}_2^T & - \end{bmatrix}. \quad (4.8)$$

\mathcal{M} is the metric implied by the mesh [16], the columns of V are the (orthonormal) left singular vectors, \hat{e}_1 and \hat{e}_2 , of the geometric Jacobian, J , and Σ is a diagonal matrix with the singular values, h_1 and h_2 , of J along the main diagonal. \mathcal{H} projects the unit circle to an ellipse with principal directions \hat{e}_1 and \hat{e}_2 and principal stretching magnitudes h_1 and h_2 [20]. Without loss of generality, we assume that the singular values are ordered such that $h_1 \leq h_2$. $\mathcal{H}^{-\alpha}$ can be expanded as

$$\mathcal{H}^{-\alpha} = V \Sigma^{-\alpha} V^T = \begin{bmatrix} | & | \\ \hat{e}_1 & \hat{e}_2 \\ | & | \end{bmatrix} \begin{bmatrix} h_1^{-\alpha} & 0 \\ 0 & h_2^{-\alpha} \end{bmatrix} \begin{bmatrix} - & \hat{e}_1^T & - \\ - & \hat{e}_2^T & - \end{bmatrix}. \quad (4.9)$$

As such, the modified regularization (4.7) limits grid motion in directions with small element length scales while allowing for greater changes in directions with larger length scales, aiding in the formation of non-degenerate high-aspect-ratio elements to resolve thin viscous structures. For simplicity, $\mathcal{H}^{-\alpha}$ is evaluated at the centroid of the given element. The metric described here is a powerful tool that can be used not only for anisotropic grid regularization but also for remeshing via a metric-based grid generator [16] in order to maintain high-quality grids, which will be the subject of future work. Moreover, we employ additional regularization operators that further inhibit element degeneration, specifically \mathcal{P}_1 grid regularization and barrier grid regularization, which are described below. Similar forms of these two regularization operators were employed in the mesh untangling algorithm by Toulorge et al. [21].

4.1.2. \mathcal{P}_1 grid regularization

To penalize excessive element curvature, the following term is added to the RHS of the objective function (4.1):

$$J_1(u) = \frac{1}{2} h_1^\beta \lambda_1 \|u - \Pi_1 u\|^2, \quad (4.10)$$

where λ_1 is the corresponding regularization coefficient, h_1 is obtained from the mesh-implied metric, Π_1 denotes the projection to a (multi-)linear subspace of U_h , and $\beta > 0$ is a parameter. The h_1^β scaling allows for increased curvature of elements with small length scales, which is important for resolving curved shocks.

4.1.3. Barrier grid regularization

Another term added to the RHS of the objective function (4.1) is the following barrier regularization:

$$J_b(u) = \frac{1}{2} \lambda_b \|f(\nabla u)\|^2, \quad (4.11)$$

where λ_b is the corresponding regularization coefficient and f is defined as

$$f(\nabla u) = \max\{0, \mathcal{J}_b - \det(\nabla u)\}, \quad (4.12)$$

with \mathcal{J}_b represents a desired lower bound on the Jacobian determinant (e.g., 10^{-10}). The regularization (4.11) penalizes invalid elements (i.e., elements for which the determinant of the geometric Jacobian is nonpositive). Though not used in this work, a log-barrier function of the form [21]

$$f(\nabla u) = \log(\det(\nabla u) - \mathcal{J}_b),$$

which, unlike the barrier function (4.12), is nonzero for $\det(\nabla u) > \mathcal{J}_b$, can also be employed.

4.1.4. Global scaling

In this work, the regularization coefficients λ_u , $\lambda_{\Delta u}$, λ_1 , and λ_b are scaled by the residual magnitude, $\|e_h(y, \sigma, u)\|$. Early in the simulation, when the residual is large and spurious transients may appear in the solution, the higher regularization prevents excessive grid changes that would otherwise occur. As the solution converges and these transients disappear, the lower regularization encourages greater adjustments to the grid to facilitate resolution of high-gradient features. To prevent rank deficiency of the linear system at low residuals, we select a small, positive number as a lower bound on λ_u (e.g., 10^{-7}).

4.2. Adaptive, elementwise regularization

Even with manual tuning, the aforementioned global, static scaling of the regularization terms is not sufficiently robust for preventing cell degeneration, especially as highly anisotropic, curved elements form to resolve multidimensional, high-gradient features. Local grid operations, whether topology-preserving (e.g., vertex smoothing [22]) or topology-changing (e.g., edge refinement, collapse [23], and swapping [22]), may be beneficial if used sparingly; however, such operations often fail to recover valid cells and will inhibit iterative convergence of the solver since they are not intrinsic to the formulation (i.e., they are applied as a “postprocessing” step at the end of the iteration). This obstruction of convergence is exacerbated in the viscous setting, wherein high-aspect-ratio elements are gradually compressed to better resolve thin viscous structures. Mesh deformation techniques have also been developed to improve mesh quality and untangle invalid elements, typically in the context of a posteriori high-order mesh generation. Examples include elasticity-based methods [24, 25, 26], in which a set of elasticity equations is solved to obtain a mesh-displacement field, and mesh optimization algorithms [21, 27], which seek to minimize element distortion and constrain invalid Jacobians via regularization operators similar to (4.10) and (4.11). Although more reliable for recovering valid elements and potentially useful for occasionally “resetting” the grid in case convergence begins to stall, these mesh-deformation techniques can be expensive and again disrupt solver convergence, especially because they need to be engaged frequently in the presence of curved, high-gradient features. Incorporating regularization operators directly into the objective function (4.1) eliminates, or at

least mitigates, obstruction of iterative convergence, but, as previously mentioned, global, static scaling of the regularization terms does not provide sufficient robustness.

In light of the above, we propose a strategy for maintaining grid validity that can reliably recover valid cells while avoiding disruption of solver convergence. In particular, when a cell becomes invalid, the iteration is restarted (i.e., the solution is “rolled back”) and the regularization coefficients are automatically adjusted in an elementwise fashion until the solver can proceed with a valid grid. In this work, $\lambda_{\Delta u}$, λ_1 , and λ_b are dynamically scaled; however, if the aspect ratio is high (e.g., $h_2/h_1 > 10$), then λ_1 is left unchanged in order to facilitate resolution of thin, curved features using curved cells. The regularization coefficients are then successively decreased to their base values, unless the element once again becomes invalid. The rollback of the solution is crucial for ensuring a valid grid at every iteration. Although our formulation does not necessarily diverge in the presence of (slightly) negative Jacobian determinants, maintaining grid validity at every iteration is important for the following reasons: (a) allowing the solver to proceed with invalid cells can result in pollution of solution accuracy and lower-quality grids that may drive the solution towards a less-optimal local minimum; (b) in our experience, once the solver proceeds with negative Jacobian determinants, it can be extremely difficult to eliminate them; and (c) potential future modifications to the formulation may result in solver blowup in the presence of *any* negative Jacobian determinants. Furthermore, although the intermittent scaling of the barrier grid regularization can cause abrupt increases in the objective function (specifically, J_b), this is not a major concern since we are ultimately interested in minimizing $\|e_h(y, \sigma, u)\|$. This adaptive, elementwise regularization strategy is found to be critical for preventing cell degeneration in the vicinity of viscous shocks and boundary layers at hypersonic flow conditions. With such high-gradient features, one to three rollbacks per iteration are typically required to preserve grid validity. Note that if the solution is rolled back, only the regularization terms need to be recomputed. The implementation details of this strategy will be provided in Section 4.4.

4.3. Increment limiting

The consideration of very strong shocks without artificial dissipation often leads to undershoots and overshoots in pressure and other quantities during intermediate iterations. To mitigate these instabilities, which can otherwise cause solver divergence, we employ an increment-limiting strategy used in standard implicit-DG solvers [17], in which the increment is scaled by a factor no greater than unity such that the maximum change in pressure and density at the integration points is less than a user-specified fraction, denoted f (e.g., $f = 10\%$). The implementation details will be provided in Section 4.4.

We have also experimented with projecting the state in troubled elements to a first-order approximation (\mathcal{P}_0), but this can hinder iterative convergence by creating a cycle in which first-order projections are followed by eventual reappearance of undershoots/overshoots, which then causes additional first-order projections, and so on. Applying sophisticated limiters that, for example, nominally preserve order of accuracy to troubled elements during intermediate iterations may also be useful, but is not considered in this work.

4.4. Line search

The solver strategies discussed in Sections 4.2 and 4.3 are incorporated into a simple line search method, as presented in Algorithm 1. It should be noted that decreasing $\|e_h(y, \sigma, u)\|$ and maintaining grid validity (i.e., minimizing J_b) are often at odds with each other since penalizing small Jacobian determinants can hinder resolution of high-gradient features, especially those which are curved. Barrier regularization is thus activated only when necessary and in a local, gradual fashion in order to avoid interfering with reduction of $\|e_h(y, \sigma, u)\|$ and potential convergence towards a less optimal local minimum. The local regularization coefficients $\lambda_{\Delta u}^\kappa$, λ_1^κ , and λ_b^κ are then successively decreased every few steps towards their base values and \mathcal{J}_b^κ is reset, provided that the given element remains valid. Recommended base values for the regularization coefficients and other parameters are given in Table 1. We also find that even though scaling the regularization coefficients by $\|e_h(y, \sigma, u)\|$ is often beneficial, sometimes, at low values of $\|e_h(y, \sigma, u)\|$, the grid has already repositioned itself enough to resolve the anisotropic structures in the flow, at which point anything more than marginal adjustments to the grid can slow down residual convergence. To minimize grid motion in this situation, λ_u and $\lambda_{\Delta u}$ are automatically scaled in a global fashion by factors of 100 for a

Table 1: Recommended base values for regularization coefficients and other parameters

λ_u	$\lambda_{\Delta u}$	λ_1	λ_b	\mathcal{J}_b	α	β
10^{-7}	10^{-5}	10^{-3}	10^2	10^{-10}	-1	3

prescribed number of iterations (e.g., 30) when repeatedly low values of the increment factor (e.g., $\omega < 0.02$) are accompanied by at least one rollback, which serves as a reliable indicator of said scenario.

Note that modifying the hard-coded values in Algorithm 1 (e.g., setting N_{search} to five and scaling $\lambda_{\Delta u}^\kappa$ by a factor of ten) can potentially yield better performance; nevertheless, the chosen values work sufficiently well for the problems considered in this study, and we remark that the primary concern of this work is robustness in terms of maintaining grid validity. Future work will explore strategies to accelerate iterative convergence, as well as well-established methods to automatically adjust the global values of λ_u and/or $\lambda_{\Delta u}$ at each step [28, 9]. In addition, though not employed here, it may be useful to activate barrier regularization over a localized region of elements, instead of just one element, since doing so for only one element can lead to movement of grid points that then causes degeneration in neighboring cells.

5. Results

We apply MDG-ICE, equipped with the enhanced solver strategies described in Section 4, to compute viscous flows with high-gradient features. Unsteady solutions are obtained using a space-time discretization. The simulations in this study are performed using the JENRE® Multiphysics Framework employed in previous work [1, 2, 3] with the modifications and extensions described here. The three-dimensional solutions are computed using hybrid shared- and distributed-memory parallelism, the latter of which was not implemented in previous work. In the present study, we employ a sparse, direct LDLT solver provided by the MUMPS (MULTifrontal Massively Parallel Solver) package [29, 30] via the PETSc (Portable, Extensible Toolkit for Scientific Computation) software library [31, 32]. Future work will improve the efficiency of solving the linear system by leveraging techniques such as domain decomposition and multigrid algorithms.

5.1. Space-time Burgers viscous shock formation

This section presents results for space-time Burgers viscous shock formation, previously computed using MDG-ICE in [2]. The initial condition is given by

$$y(x, t = 0) = \frac{1}{2\pi t_s} \sin(2\pi x) + y_\infty, \quad (5.1)$$

where $t_s = 0.5$ is the time of shock formation and $y_\infty = 0.2$ is the freestream velocity. The computational domain is $\Omega = [0, 1] \times [0, 1]$. Inflow and outflow boundary conditions are applied at the left and right boundaries, respectively. The solution is initialized by extruding the initial condition (5.1) in the temporal direction. We employ continuation in μ , i.e., a series of problems is solved in which μ is successively decreased, with the final solution of a given problem used as the initial condition of the subsequent one. In previous work [2], MDG-ICE(\mathcal{P}_5) solutions were computed, also with μ continuation. Specifically, viscosities of $\mu = 10^{-3}$, $\mu = 5 \times 10^{-4}$, and $\mu = 10^{-4}$ were considered. The initial grid consisted of 200 linear triangular elements obtained by splitting each element of a uniform 10×10 quadrilateral mesh into two triangles, resulting in a regular topology. Here, we compute MDG-ICE(\mathcal{P}_5) solutions for a more challenging series of viscosities: $\mu = 10^{-3}$, $\mu = 10^{-4}$, and $\mu = 10^{-5}$. We employ two different grids: the first is the same as in [2] (i.e., a regular grid with 200 triangular elements), while the second is an irregular grid with 242 triangular elements. A key difference with [2] is that the elements are of quadratic geometric order, significantly increasing the difficulty of achieving solution convergence while maintaining a valid grid.

Algorithm 1 Line search algorithm for iteration $i + 1$. $\omega \leq 1$ is a positive factor that scales the increment. The κ superscripts denote element-local quantities. $\mathcal{J}_{\min}^\kappa$ is the minimum Jacobian determinant for cell κ . The compressible Navier-Stokes system is assumed (Section 2.2).

Input: $(y, \sigma, u)_i$

```

converged  $\leftarrow$  False
while not converged do
  Compute  $\Delta(y, \sigma, u)_i$ 
   $\omega \leftarrow 1$ ,  $\omega_a \leftarrow 0$ ,  $\omega_b \leftarrow 1$ 
   $(y, \sigma, u)^* \leftarrow (y, \sigma, u)_i$ 
   $N_{\text{search}} \leftarrow 5$ 
  for  $k \leftarrow 0$  to  $N_{\text{search}}$  do
    if  $k > 0$  then
       $\omega \leftarrow (\omega_a + \omega_b)/2$ 
    end if
     $(y, \sigma, u)_{i+1} \leftarrow (y, \sigma, u)_i + \omega \Delta(y, \sigma, u)_i$ 
     $F_\rho \leftarrow \max_\Omega \{|\rho_{i+1} - \rho_i|/\rho_i\}$ 
     $F_P \leftarrow \max_\Omega \{|P(y_{i+1}) - P(y_i)|/P(y_i)\}$ 
    if  $\|e_h(y, \sigma, u)_{i+1}\| / \|e_h(y, \sigma, u)^*\| < 1$  and  $F_\rho \leq f$  and  $F_P \leq f$  then
      if  $\omega = 1$  then
        break
      end if
       $(y, \sigma, u)^* \leftarrow (y, \sigma, u)_{i+1}$ 
       $\omega_a \leftarrow \omega$ 
    else
       $\omega_b \leftarrow \omega$ 
    end if
    if  $\omega_a = 0$  and  $N_{\text{search}} = 5$  then
       $N_{\text{search}} \leftarrow N_{\text{search}} + 10$   $\triangleright$  Could not reduce  $\|e_h(y, \sigma, u)\|$ ; increase  $N_{\text{search}}$ 
    end if
  end for
   $(y, \sigma, u)_{i+1} \leftarrow (y, \sigma, u)^*$ 
  converged  $\leftarrow$  True
  for each element  $\kappa$  do
    if  $\mathcal{J}_{\min}^{\kappa, i+1} < \mathcal{J}_b^\kappa$  then
      converged  $\leftarrow$  False
       $\lambda_{\Delta u}^\kappa \leftarrow 10\lambda_{\Delta u}^\kappa$ ,  $\lambda_b^\kappa \leftarrow 10\lambda_b^\kappa$ ,  $\lambda_1^\kappa \leftarrow 100\lambda_1^\kappa$ 
       $\mathcal{J}_b^\kappa \leftarrow 10\mathcal{J}_{\min}^{\kappa, i}$ 
    end if
  end for
end while

```

5.1.1. Initial mesh topology: Regular

Figure 5.1a presents the space-time initial condition and final solutions for $\mu = 10^{-3}$, $\mu = 10^{-4}$, and $\mu = 10^{-5}$, with the corresponding grids superimposed. Figure 5.2 shows the corresponding one-dimensional profiles at $t = 0.025$ and $t = 0.975$. MDG-ICE automatically adjusts the grid geometry to resolve the viscous shock as a sharp yet smooth profile without relying on artificial stabilization or mesh-topology modification. As the viscosity is decreased, the viscous shock becomes thinner and the aspect ratios of the nearby elements are increased via anisotropic space-time r -adaptivity. The solutions are free from spurious oscillations. The nonlinear-solver strategies described in Section (4) enable excellent resolution of the thin viscous shock while maintaining grid validity.

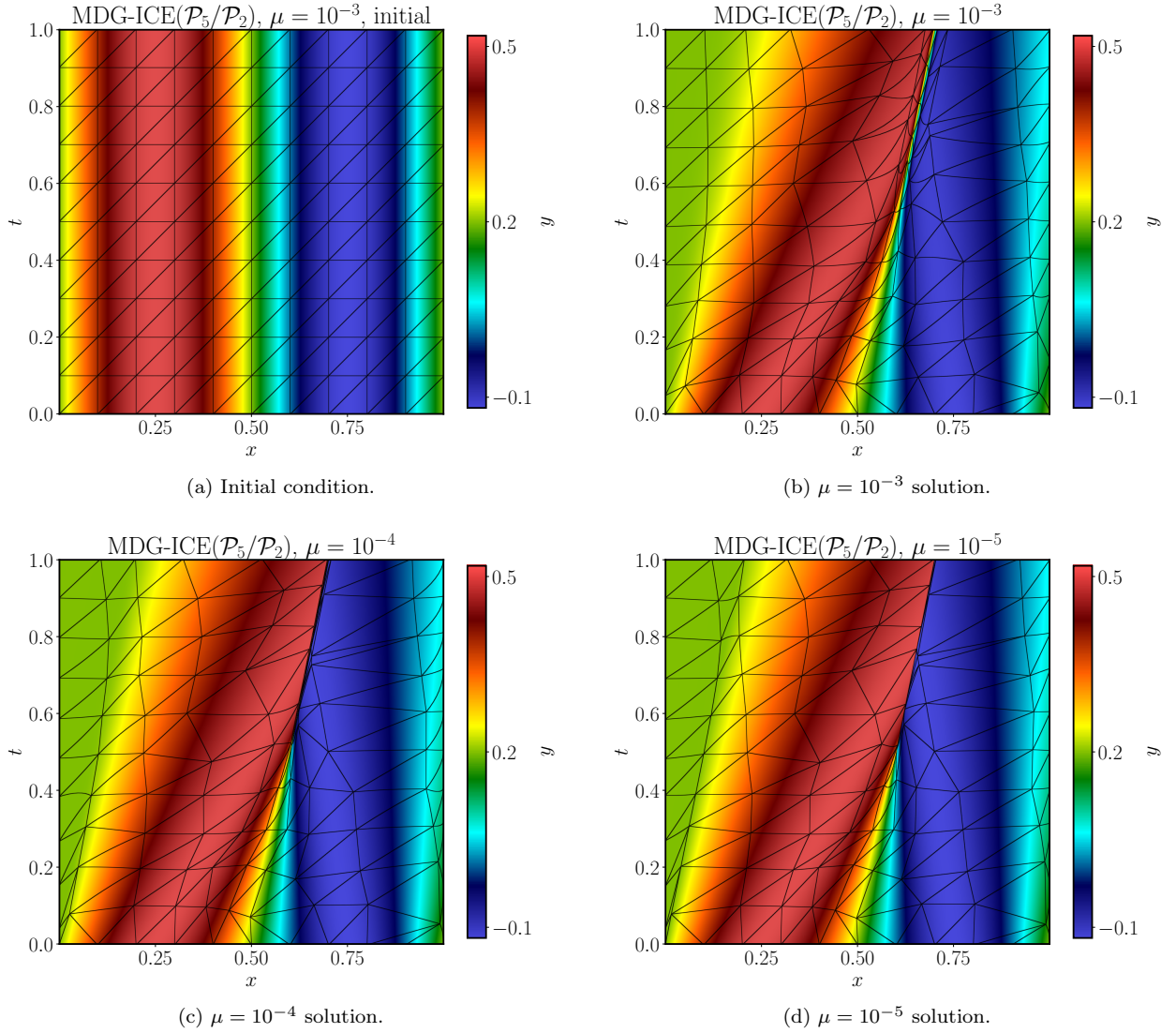
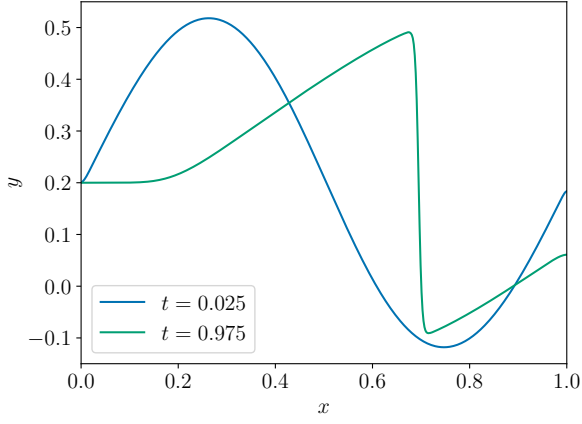
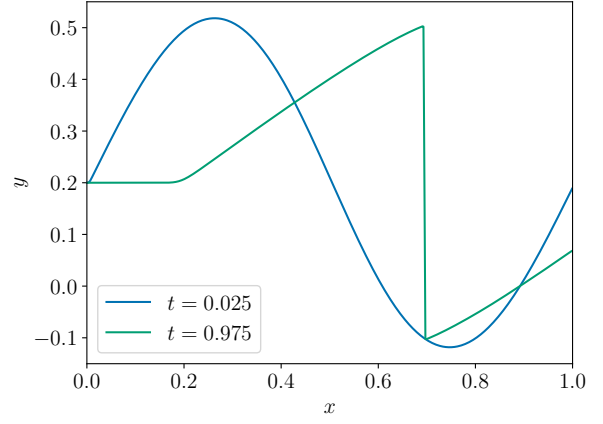


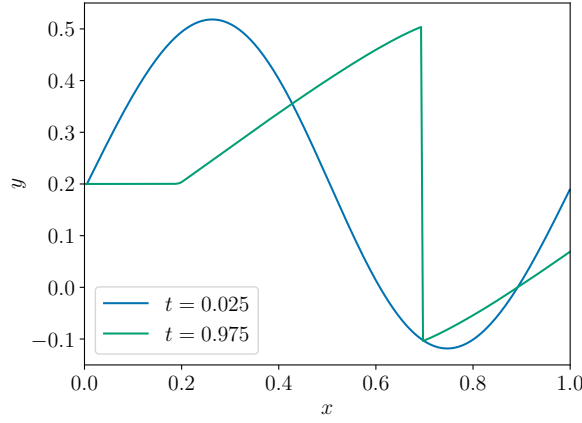
Figure 5.1: The space-time Burgers initial condition and final solutions for $\mu = 10^{-3}$, $\mu = 10^{-4}$, and $\mu = 10^{-5}$, with the corresponding grids superimposed. The initial grid consists of 200 triangular elements of quadratic geometric order with a regular topology. The initial condition is given in Equation (5.1).



(a) $\mu = 10^{-3}$ solution.



(b) $\mu = 10^{-4}$ solution.



(c) $\mu = 10^{-5}$ solution.

Figure 5.2: One-dimensional profiles at $t = 0.025$ and $t = 0.975$ for $\mu = 10^{-3}$, $\mu = 10^{-4}$, and $\mu = 10^{-5}$ for space-time Burgers viscous shock formation. The initial grid consists of 200 triangular elements of quadratic geometric order with a regular topology. The initial condition is given in Equation (5.1).

The nonlinear convergence history is given in Figure 5.3. The initial residual magnitudes for the $\mu = 10^{-4}$ and $\mu = 10^{-5}$ simulations are relatively small since the solver is restarted from the corresponding higher-viscosity solution.

5.1.2. Initial mesh topology: Irregular

The initial 242-element irregular grid, along with the initial condition, is displayed in Figure 5.4a. The final solutions and grids for $\mu = 10^{-3}$, $\mu = 10^{-4}$, and $\mu = 10^{-5}$ are given in Figures 5.4b, 5.4c, and 5.4d, respectively. Figure 5.5 presents the corresponding one-dimensional profiles at $t = 0.025$ and $t = 0.975$. Similar to the regular-topology case, MDG-ICE automatically modifies the location, size, and orientation of elements to resolve the viscous shock via anisotropic space-time r -adaptivity. Additional grid adjustments are introduced accordingly as the viscosity is decreased and the shock becomes more difficult to resolve. The final solutions are well-resolved and free from spurious oscillations. The nonlinear convergence history is displayed in Figure 5.6.

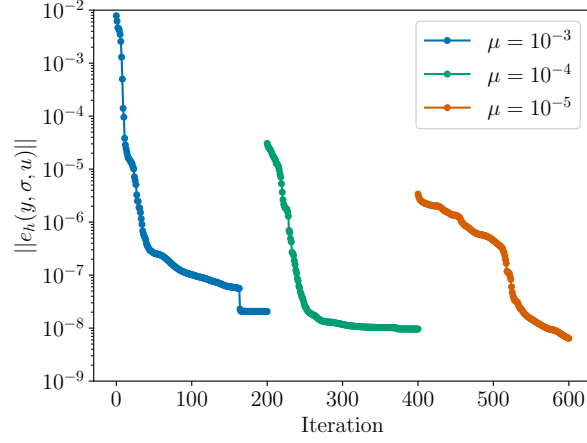


Figure 5.3: Nonlinear convergence history for space-time Burgers viscous shock formation. The initial grid consists of 200 triangular elements of quadratic geometric order with a regular topology. The initial condition is given in Equation (5.1).

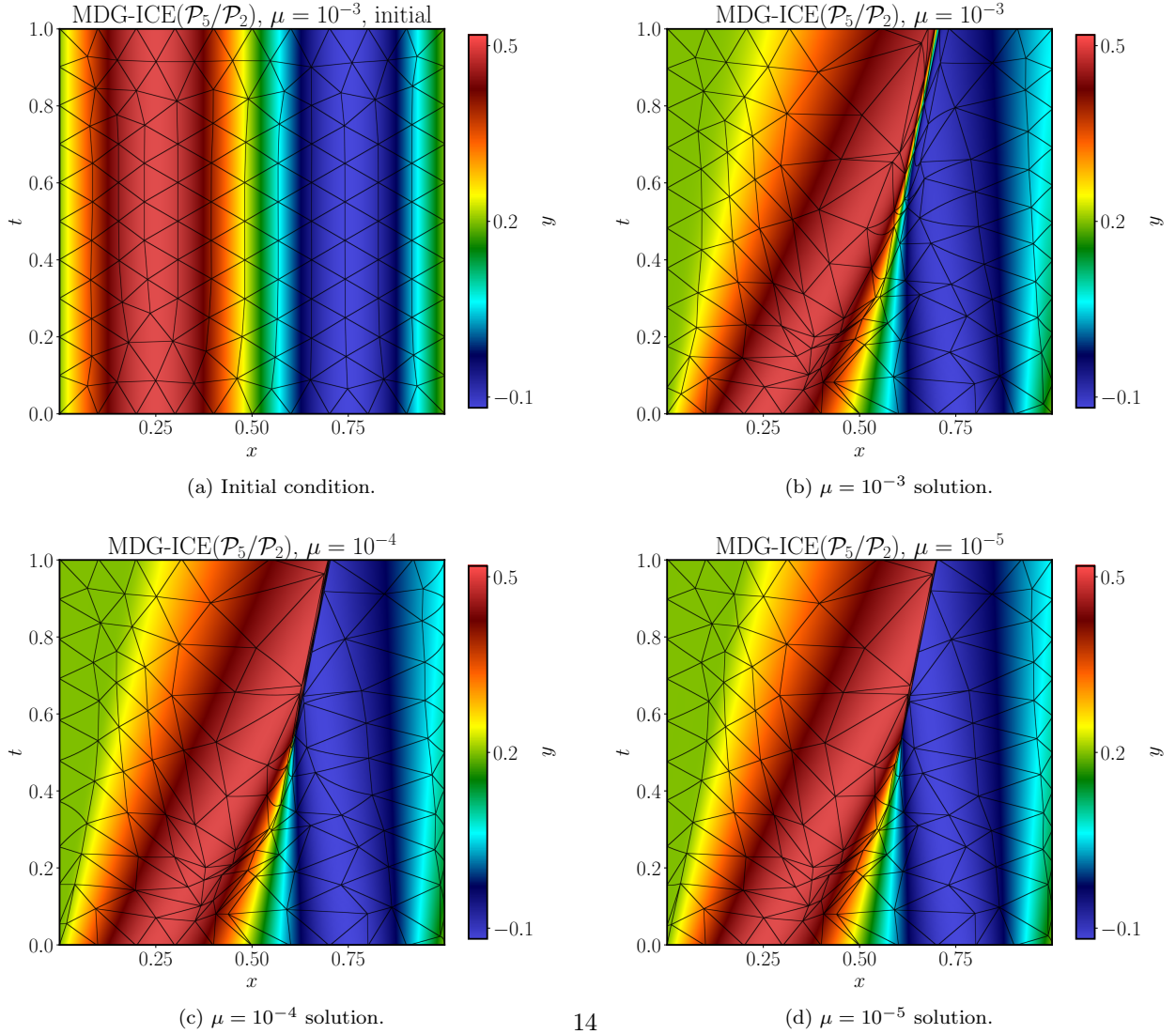


Figure 5.4: The space-time Burgers initial condition and final solutions for $\mu = 10^{-3}$, $\mu = 10^{-4}$, and $\mu = 10^{-5}$, with the corresponding grids superimposed. The initial grid consists of 242 triangular elements of quadratic geometric order with an irregular topology. The initial condition is given in Equation (5.1).

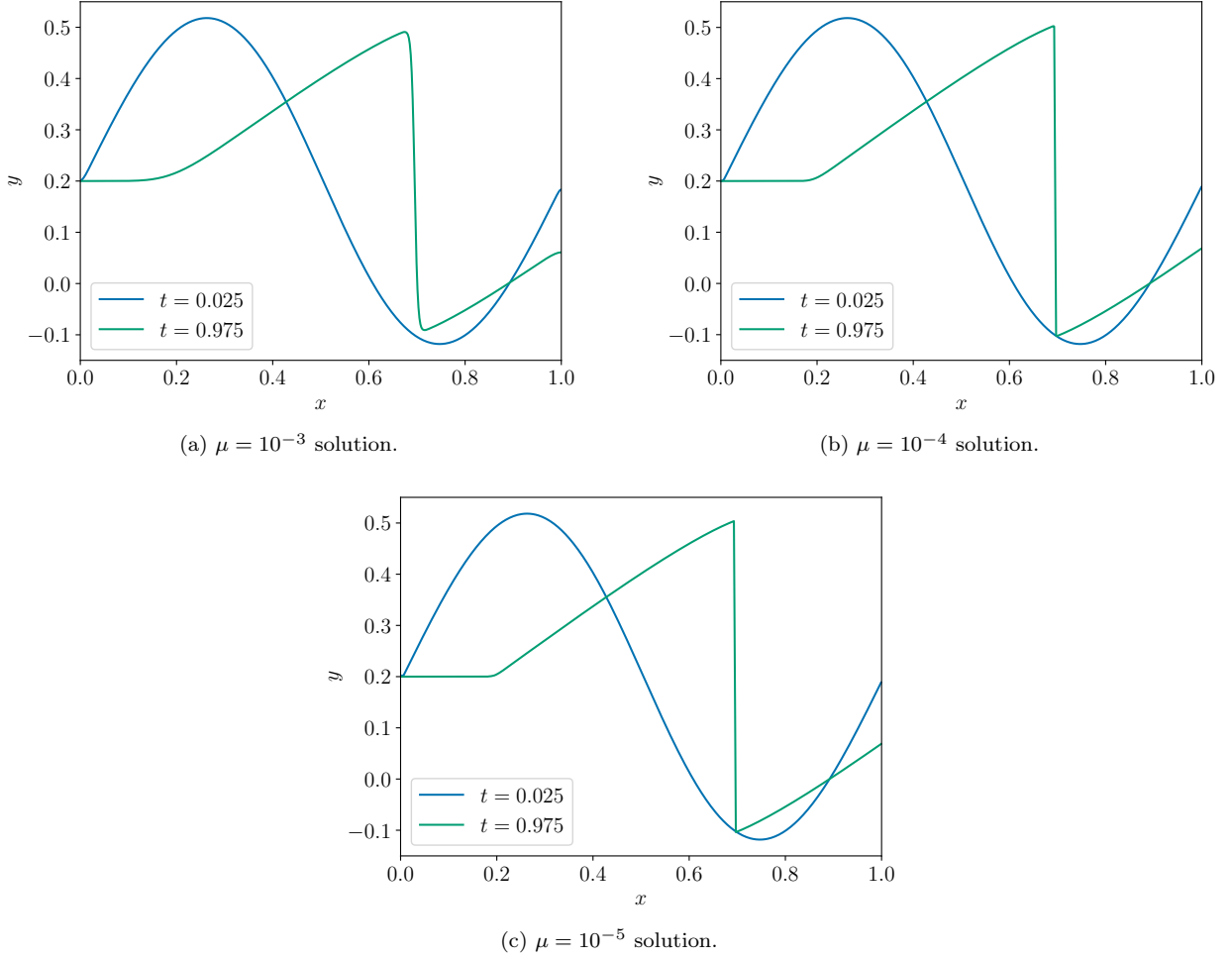


Figure 5.5: One-dimensional profiles at $t = 0.025$ and $t = 0.975$ for $\mu = 10^{-3}$, $\mu = 10^{-4}$, and $\mu = 10^{-5}$ for space-time Burgers viscous shock formation. The initial grid consists of 242 triangular elements of quadratic geometric order with an irregular topology. The initial condition is given in Equation (5.1).

5.2. Mach 17.6 flow over two-dimensional cylinder

Next, we compute steady hypersonic viscous flow over a circular half-cylinder in two spatial dimensions. The freestream Mach number and Reynolds number (based on the cylinder radius) are 17.6 and 376,930, respectively. This problem is a common benchmark case for evaluating the ability of numerical techniques to predict hypersonic flows. With conventional finite volume techniques [14, 15], significant asymmetries in the surface heat-flux profile were observed on both regular and irregular simplicial grids. Note that fairly symmetric heating results have been obtained on simplicial grids with DG schemes equipped with smooth artificial viscosity [33, 7]. In this work, we aim to use the proposed MDG-ICE formulation to achieve symmetric solutions without artificial dissipation. We employ two different starting grids: the first is a regular grid with 388 elements, while the second is an irregular grid with 526 elements. Freestream conditions are imposed at the inflow boundary, defined as the ellipse $(x/6)^2 + (y/3)^2 = 1$. Extrapolation is employed at the outflow boundary, and the cylinder boundary, a half-circle of unit radius, is an isothermal no-slip wall with temperature $T_{\text{wall}} = 2.5T_{\infty}$, where $(\cdot)_{\infty}$ denotes freestream conditions.

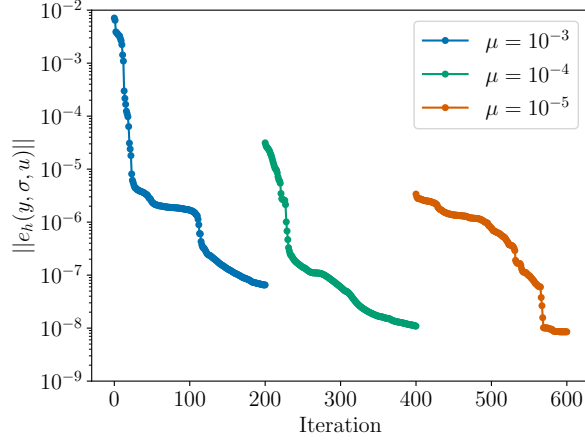


Figure 5.6: Nonlinear convergence history for space-time Burgers viscous shock formation. The initial grid consists of 242 triangular elements of quadratic geometric order with an irregular topology. The initial condition is given in Equation (5.1).

5.2.1. Initial mesh topology: Regular

We employ continuation in both the Mach number and the Reynolds number, starting with an isoparametric MDG-ICE(\mathcal{P}_4) solution corresponding to $\text{Ma} = 5, \text{Re} = 500$. This MDG-ICE solution is initialized with a conventional DG solution stabilized with elementwise-constant artificial viscosity of the form described in [34]. Keeping Re fixed at 500, the Mach number is consecutively increased by increments of one until the target value of 17.6 is reached. These intermediate solutions are not fully converged to a stationary point. The 388-element mesh and temperature field for the $\text{Ma} = 17.6, \text{Re} = 500$ solution are presented in Figure 5.7. The elements in the vicinity of the shock are anisotropic yet still valid. The MDG-ICE solution is free from oscillations even in the absence of artificial dissipation.

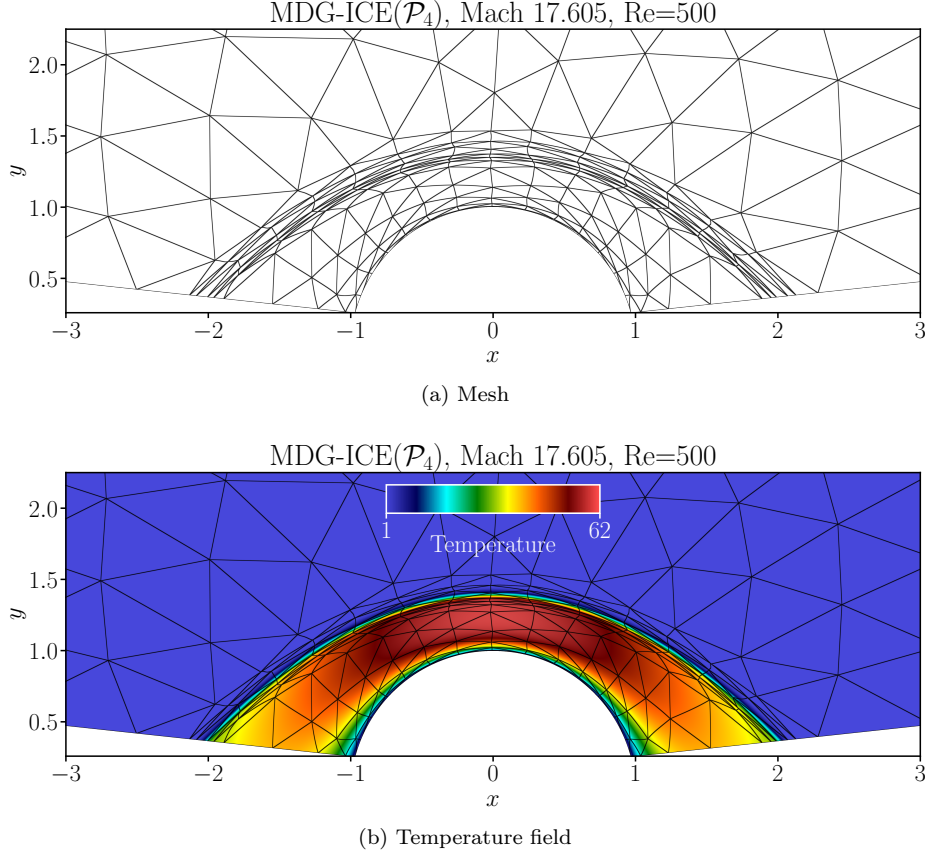


Figure 5.7: The MDG-ICE solution computed using 388 \mathcal{P}_4 isoparametric triangle elements for for two-dimensional Mach 17.6 flow over a cylinder at $\text{Re} = 500$. The initial grid has a regular topology.

The Reynolds number is then consecutively increased by factors of approximately two until the target value of 376,930 is reached. At this Reynolds number, we increase the polynomial degrees of Y_h and Σ_h from four to five in order to eliminate slight asymmetries in the surface heat-flux profile, as will be shown later in this section. The final mesh and temperature, Mach, and pressure fields are given in Figure 5.8. Considerable jumps in temperature and pressure are observed. MDG-ICE automatically adjusts the grid geometry in order to resolve the viscous shock and boundary layer, which become sharper as the Reynolds number is increased. Highly anisotropic elements are observed at the shock and in the boundary layer, yet grid validity is maintained. The solution is well-resolved and free from spurious artifacts. Despite the initially regular nature of the mesh, there is undoubtedly very strong misalignment between the grid and the shock and boundary layer. Figure 5.9 displays the nonlinear convergence history for the subparametric MDG-ICE($\mathcal{P}_5/\mathcal{P}_4$) solution. The residual starts at a relatively small value since the simulation is restarted from an isoparametric MDG-ICE(\mathcal{P}_4) solution. Future work will focus on incorporating stabilization mechanisms (at least during early/intermediate iterations) and/or space-time marching in order to accelerate convergence and circumvent the need for continuation in Mach number and Reynolds number, which itself can be considered akin to (global) artificial dissipation. Nevertheless, this demonstrates how MDG-ICE can be naturally employed for parametric studies in which the flow conditions are varied; other grid adaptation strategies may need to incorporate coarsening techniques to maintain efficiently refined grids.

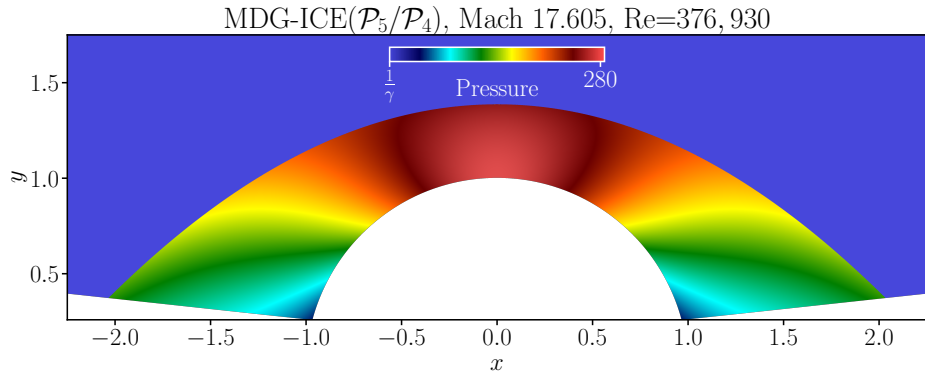
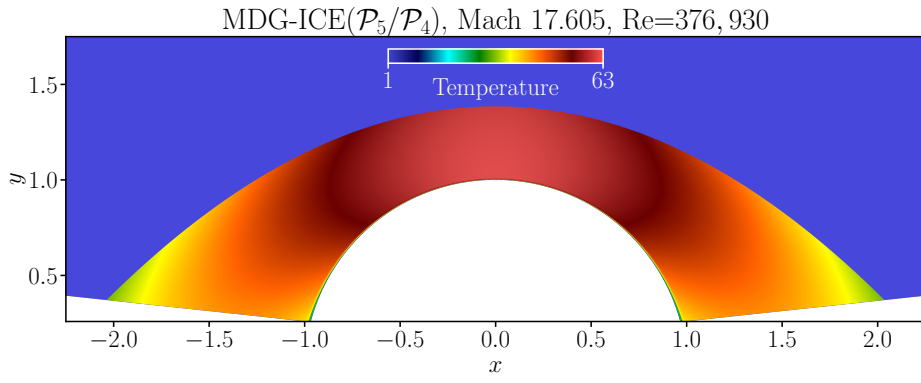
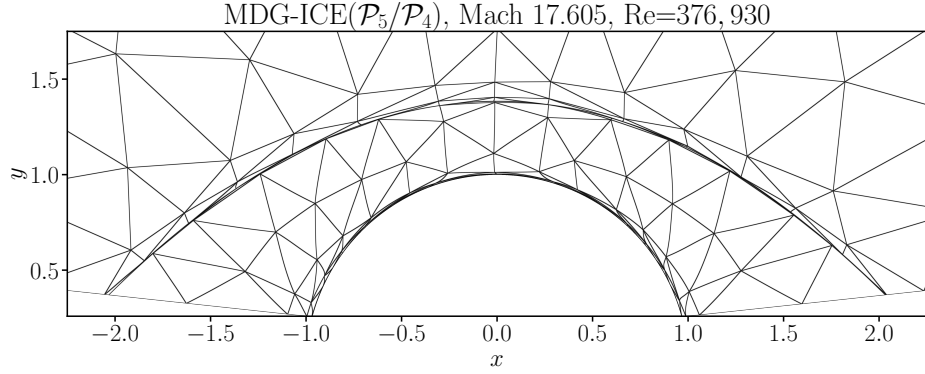


Figure 5.8: The MDG-ICE solution computed using 388 subparametric $\mathcal{P}_5/\mathcal{P}_4$ triangle elements for two-dimensional Mach 17.6 flow over a cylinder at $\text{Re} = 376,930$. The initial grid has a regular topology.

Figure 5.10 presents the isoparametric MDG-ICE(\mathcal{P}_4) and subparametric MDG-ICE($\mathcal{P}_5/\mathcal{P}_4$) predictions of the pressure coefficient and Stanton number, defined as

$$C_p = \frac{P - P_\infty}{\frac{1}{2}\rho_\infty v_\infty^2}$$

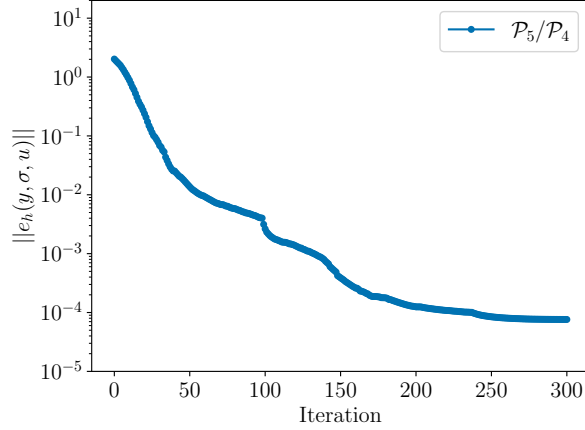


Figure 5.9: Nonlinear convergence history for the subparametric MDG-ICE($\mathcal{P}_5/\mathcal{P}_4$) solution to Mach 17.6 flow over a two-dimensional cylinder. The initial grid has a regular topology.

and

$$C_h = \frac{q_n}{c_p \rho_\infty v_\infty (T_{t,\infty} - T_{\text{wall}})},$$

respectively, where $(\cdot)_\infty$ denotes a freestream quantity, q_n is the normal heat flux, $c_p = R\gamma/(\gamma - 1)$ is the specific heat capacity at constant pressure, and T_t is the stagnation temperature. The pressure profiles for both MDG-ICE solutions are highly symmetric, but the heat-flux profile for the isoparametric MDG-ICE(\mathcal{P}_4) solution exhibits a slight nonphysical cusp at the stagnation point. Nevertheless, this cusp is eliminated with p -refinement. The stagnation-point Stanton number in the MDG-ICE($\mathcal{P}_5/\mathcal{P}_4$) solution is approximately 0.0077. Note that there exists some variation in the stagnation-point Stanton number reported in the literature; for example, 0.0085 in [15], 0.0076 in [35], and 0.0082 in [33].

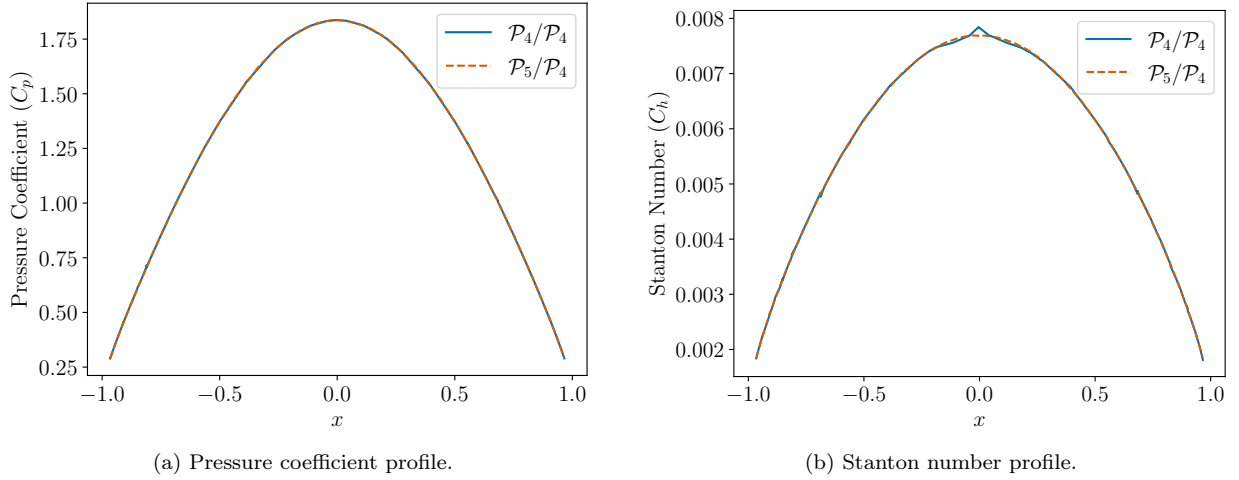


Figure 5.10: Surface profiles of pressure coefficient and Stanton number for the MDG-ICE solution computed using 388 $\mathcal{P}_5/\mathcal{P}_4$ triangle elements for two-dimensional Mach 17.6 flow over a cylinder at $\text{Re} = 376,930$. The initial grid has a regular topology.

5.2.2. Initial mesh topology: Irregular

Continuation in the Mach and Reynolds numbers is once again employed, starting with $\text{Ma} = 5$, $\text{Re} = 100$. The 526-element mesh and temperature field for an intermediate MDG-ICE solution at $\text{Ma} = 5$, $\text{Re} = 100$

are presented in Figure 5.11. The temperature field is smooth. At this low Reynolds number, only slight grid repositioning is required to resolve the flow.

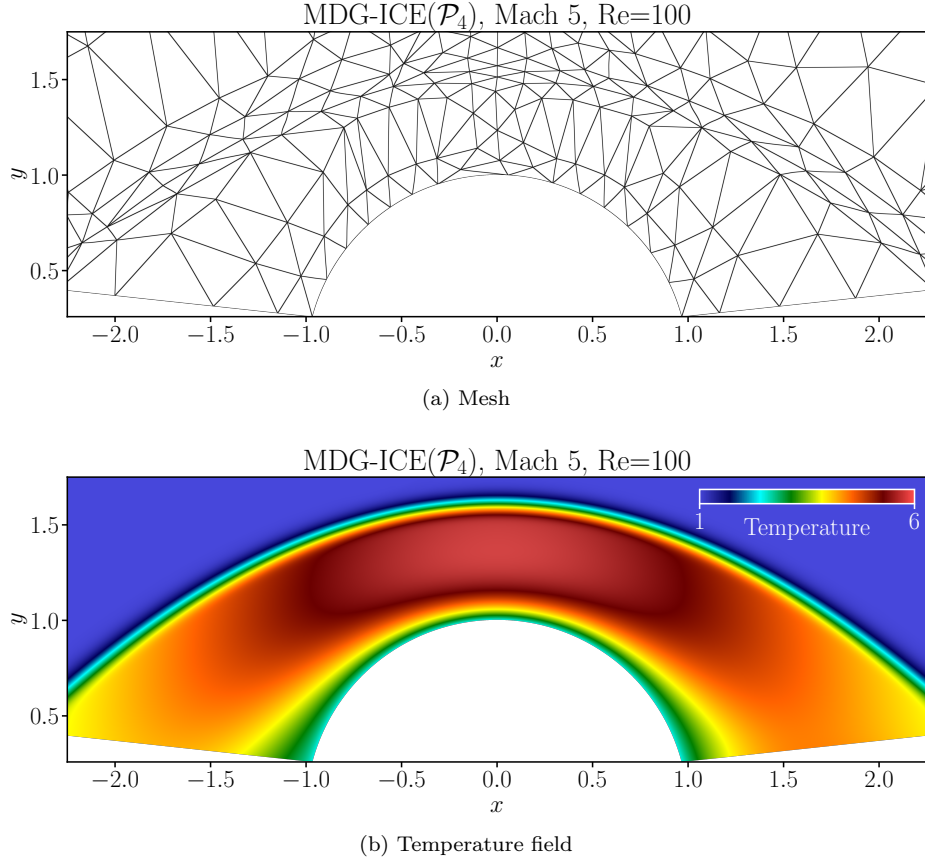


Figure 5.11: The MDG-ICE solution computed using 526 \mathcal{P}_4 isoparametric triangle elements for for two-dimensional Mach 17.6 flow over a cylinder at $\text{Re} = 100$. The initial grid has an irregular topology.

Global p -refinement of the state and auxiliary-variable approximations is again employed. The final subparametric MDG-ICE($\mathcal{P}_5/\mathcal{P}_4$) solution at $\text{Ma} = 17.6, \text{Re} = 376,930$ is given in Figure 5.12. The long, thin elements oriented orthogonal to the shock are a direct consequence of two main factors associated with the initially irregular nature of the grid: (a) moreso than in the regular case, incrementing the Mach and Reynolds numbers (in the absence of additional stabilization) causes transient artifacts to appear upstream of the shock, which then induce appreciable grid motion; (b) the compression of the grid at the shock and boundary layer is less likely to pull in outlying elements accordingly than in the regular case. Note that starting with intermediate Reynolds numbers, α is set to zero in order to alleviate excessive stiffening of the anisotropic, shock-orthogonal elements due to the Laplacian regularization (4.7). Although it is not clear how detrimental this type of element may be in more complex configurations (if at all), the formation of such elements can be mitigated by, as previously discussed, the use of artificial dissipation during intermediate iterations and/or metric-based remeshing. Nevertheless, the thin viscous structures remain sharp and free from spurious oscillations.

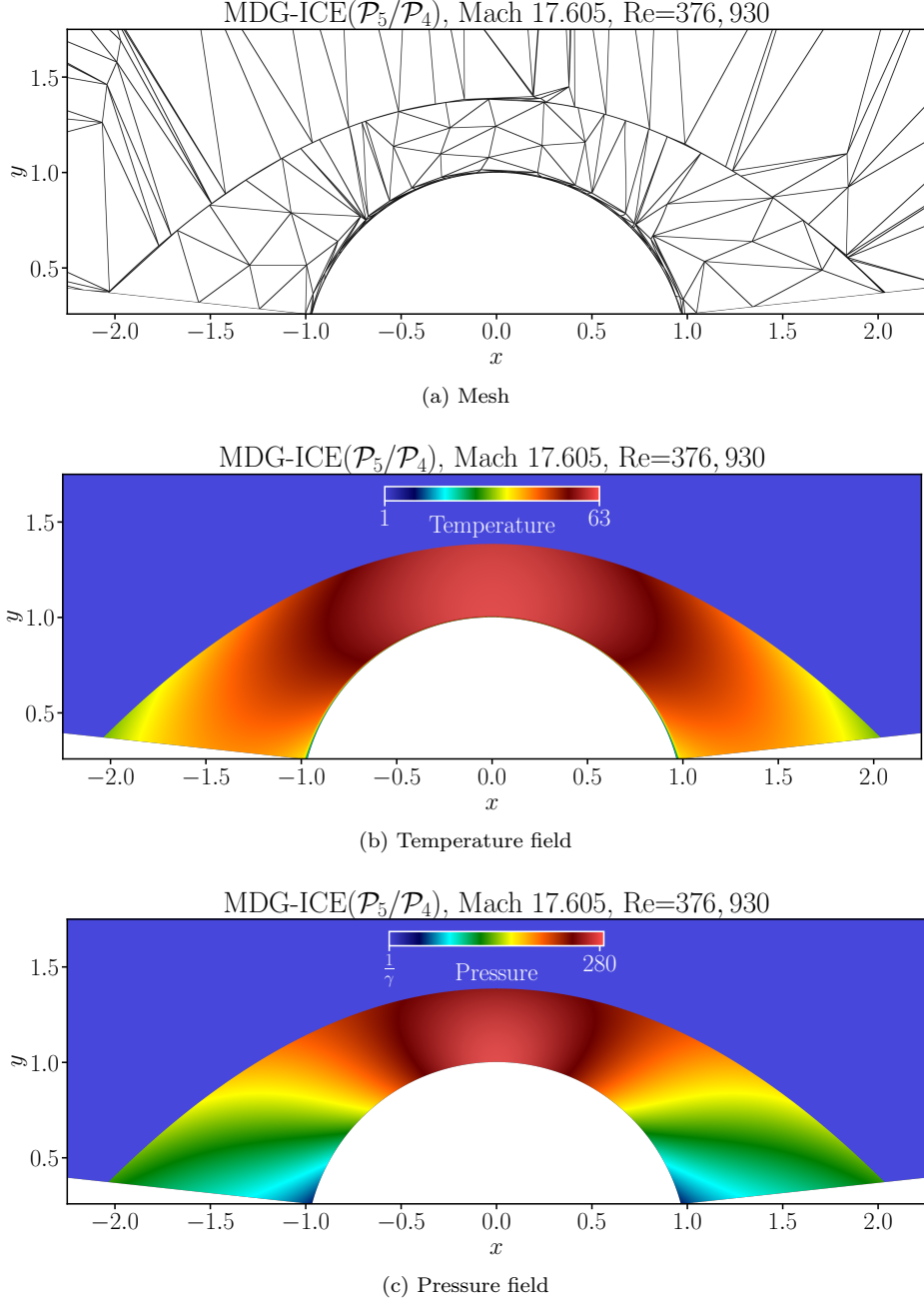


Figure 5.12: The MDG-ICE solution computed using 526 $\mathcal{P}_5/\mathcal{P}_4$ subparametric triangle elements for two-dimensional Mach 17.6 flow over a cylinder at $\text{Re} = 376,930$. The initial grid has an irregular topology.

Figure 5.9 displays the nonlinear convergence history for the subparametric MDG-ICE($\mathcal{P}_5/\mathcal{P}_4$) solution. The initial residual is already low since the simulation is restarted from an isoparametric MDG-ICE(\mathcal{P}_4) solution.

Figure 5.14 presents the surface profiles of pressure coefficient and Stanton number for the subparametric MDG-ICE($\mathcal{P}_5/\mathcal{P}_4$) solution. The stagnation-point Stanton number is approximately 0.0077. Despite the evidently asymmetric grid and extremely strong grid-shock misalignment, the surface profiles are highly

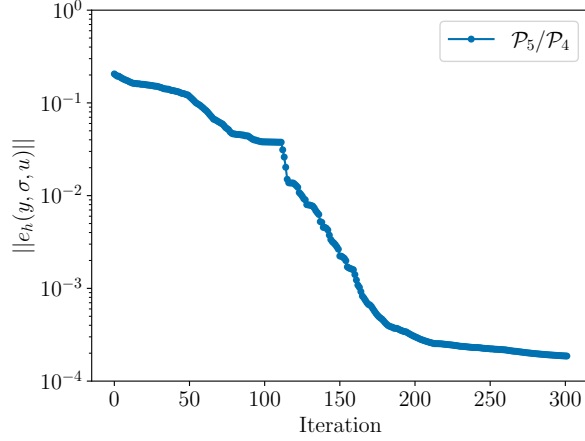


Figure 5.13: Nonlinear convergence history for the subparametric MDG-ICE($\mathcal{P}_5/\mathcal{P}_4$) solution to Mach 17.6 flow over a two-dimensional cylinder. The initial grid has an irregular topology.

symmetric and agree well with those in Figure (5.10).

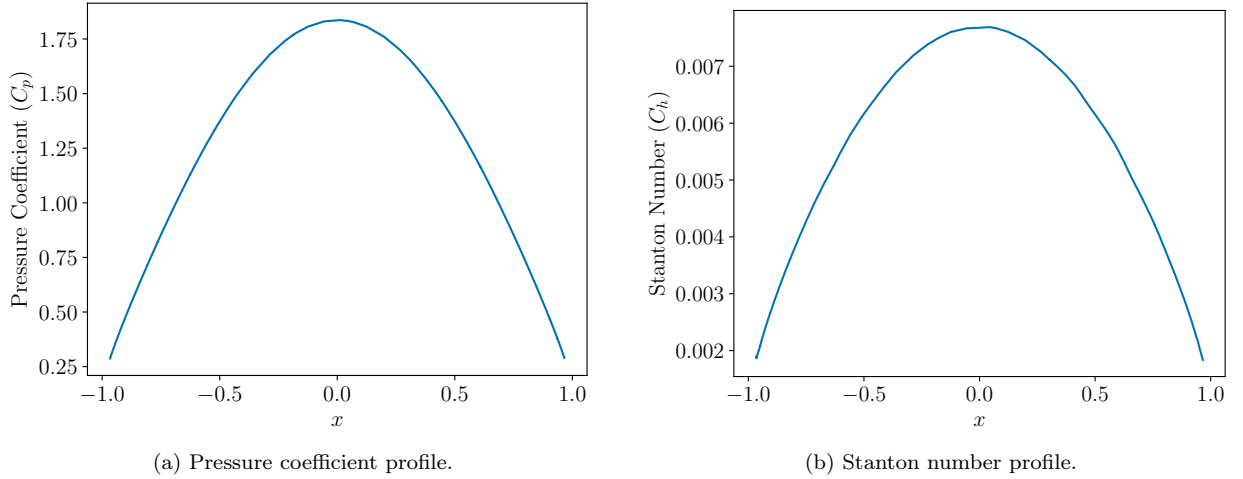


Figure 5.14: Surface profiles of pressure coefficient and Stanton number obtained with the MDG-ICE solution computed using 526 $\mathcal{P}_5/\mathcal{P}_4$ subparametric triangle elements for two-dimensional Mach 17.6 flow over a cylinder at $\text{Re} = 376,930$. The initial grid has an irregular topology.

5.3. Mach 17.6 flow over three-dimensional cylinder

This test case is the three-dimensional version of the previous configuration. The consideration of three spatial dimensions allows for the emergence of instabilities and asymmetries that are naturally suppressed in the two-dimensional case. In particular, it is with a three-dimensional domain that nonphysical artifacts in the heat-flux profiles obtained with finite volume schemes are most prominent [15, 14]. The two-dimensional domain is extruded one layer of cells in the homogeneous direction by two (nondimensional) units. Slip conditions are applied at the symmetry boundaries. Unlike in the previous subsection, the inflow boundary is defined as the circle $x^2 + y^2 = 6.5^2$. The reason for this modification is that as the Mach number is increased during the continuation strategy, spurious transients appear upstream of the shock and interact with the boundary, causing noticeable instabilities that can be dampened by positioning the inflow boundary far away from the shock. Although also present in the two-dimensional simulations, these instabilities are

exacerbated in the three-dimensional setting. Again, the use of artificial dissipation would likely resolve this issue.

An isoparametric $DG(\mathcal{P}_3)$ solution at $Ma = 14, Re = 100$ on 3024 tetrahedral cells is used as the initial condition for the MDG-ICE continuation with superparametric $\mathcal{P}_3/\mathcal{P}_4$ cells. A positivity-preserving and entropy-based linear-scaling limiter [36, 37, 38] is employed to help maintain stability in the DG solution. The temperature field and initial grid for the DG solution are presented in Figure 5.15. Note the coarseness of the grid with respect to the expected high-gradient features at the target conditions. After reaching $Ma = 17.6, Re = 376,930$, two global p -refinements of the state and auxiliary-variable approximations are performed. The final subparametric MDG-ICE($\mathcal{P}_5/\mathcal{P}_4$) solution is displayed in Figure 5.15. Just as in the two-dimensional case, the grid is automatically adapted to resolve the viscous shock and boundary layer while maintaining grid validity. Figure 5.17 zooms in on the shock layer along the stagnation line. Extremely high-aspect-ratio elements at the shock and boundary layer are observed. In particular, the cells at the shock are almost visually indistinguishable. Furthermore, in the temperature field, although the smoothness of the boundary layer can be discerned, the viscous shock resembles a truly discontinuous feature.

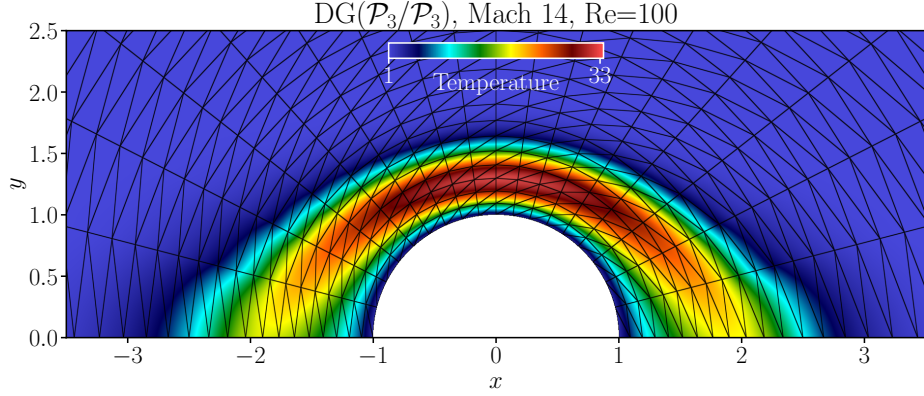


Figure 5.15: Isoparametric $DG(\mathcal{P}_3)$ solution at $Ma = 14, Re = 100$ on 3024 tetrahedral cells. This solution is used as the initial condition for the MDG-ICE continuation strategy.

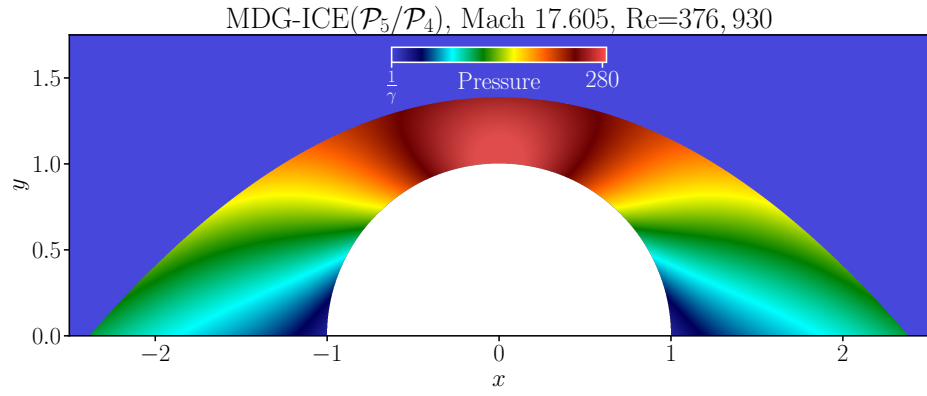
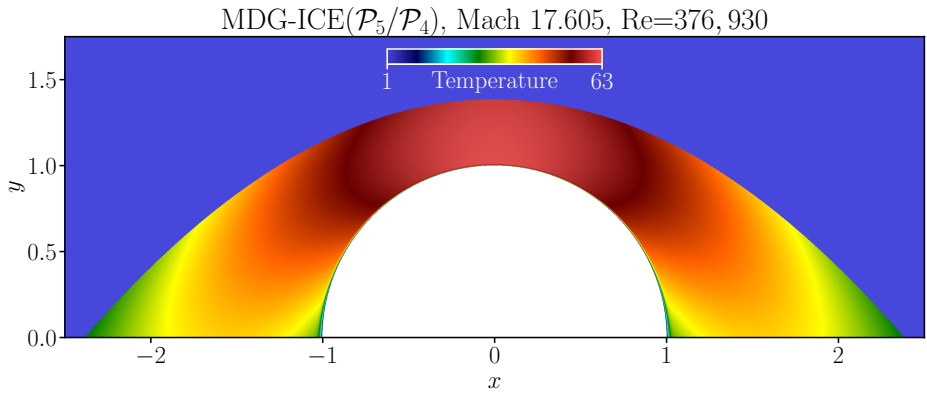
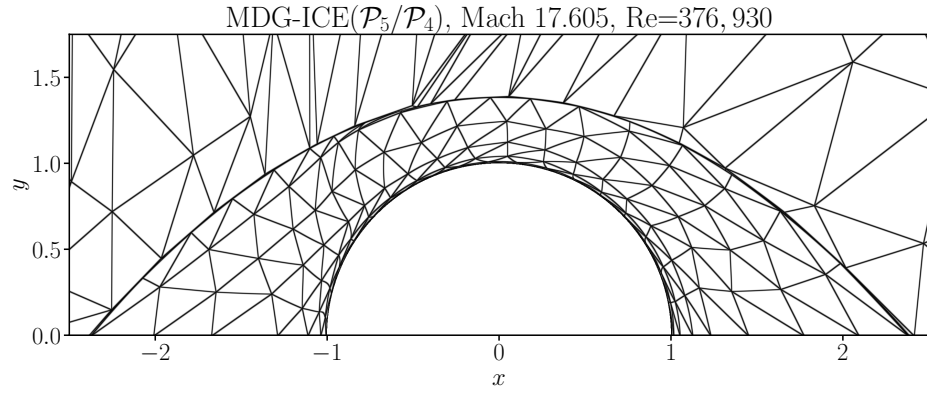


Figure 5.16: The MDG-ICE solution computed using 3024 $\mathcal{P}_5/\mathcal{P}_4$ subparametric tetrahedral elements for three-dimensional Mach 17.6 flow over a cylinder at $\text{Re} = 376,930$.

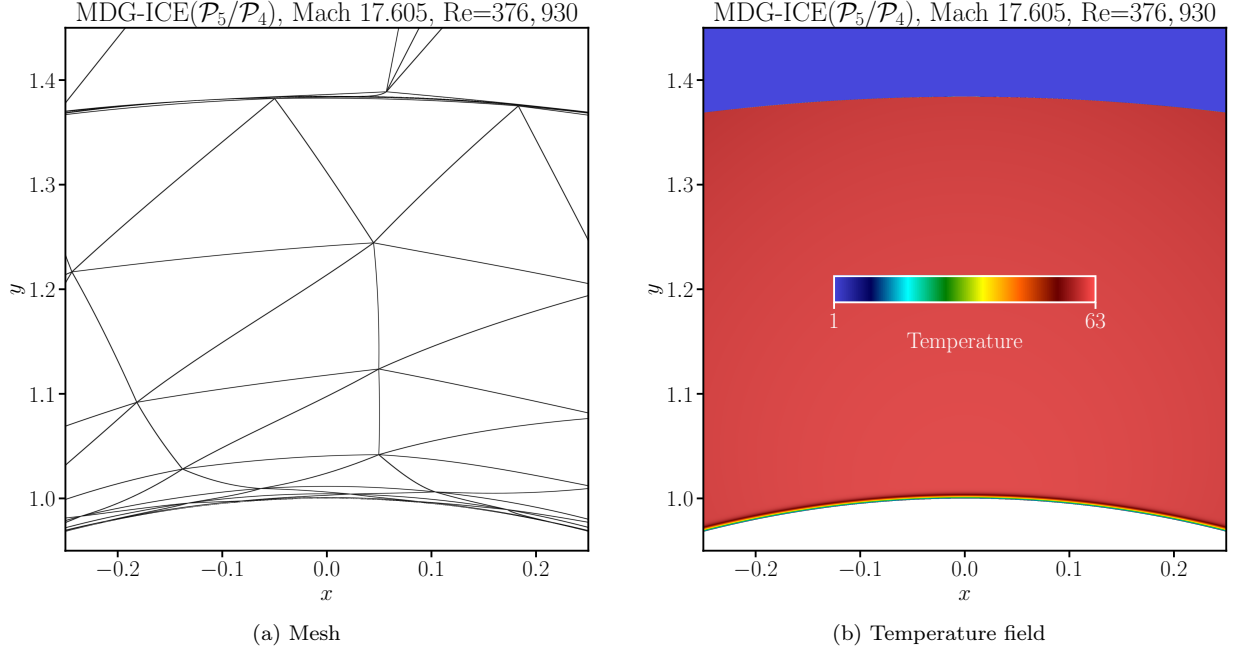


Figure 5.17: Zoomed-in view of the subparametric MDG-ICE($\mathcal{P}_5/\mathcal{P}_4$) solution to three-dimensional Mach 17.6 flow over a cylinder at $\text{Re} = 376,930$.

The convergence history for the subparametric MDG-ICE($\mathcal{P}_5/\mathcal{P}_4$) solution is given in Figure 5.18. The residual magnitude starts at a relatively small value since the solution is restarted from an isoparametric MDG-ICE($\mathcal{P}_4/\mathcal{P}_4$) calculation. Figure 5.19 shows the stagnation-line profiles of temperature and pressure. The stagnation point is located at $y = 1$. These results further confirm that the solution is free from spurious oscillations, despite the substantial gradient across the shock.

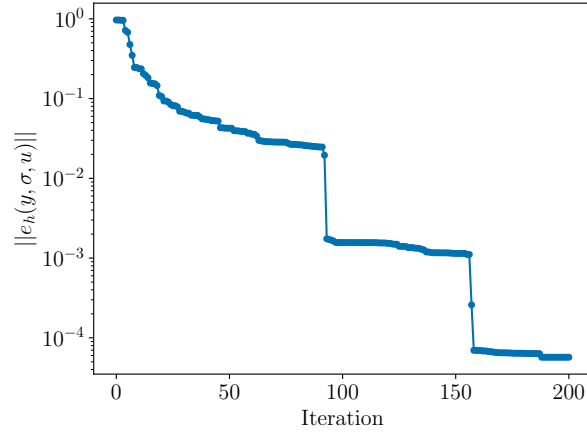


Figure 5.18: Nonlinear convergence history for the subparametric MDG-ICE($\mathcal{P}_5/\mathcal{P}_4$) solution to Mach 17.6 flow over a three-dimensional cylinder.

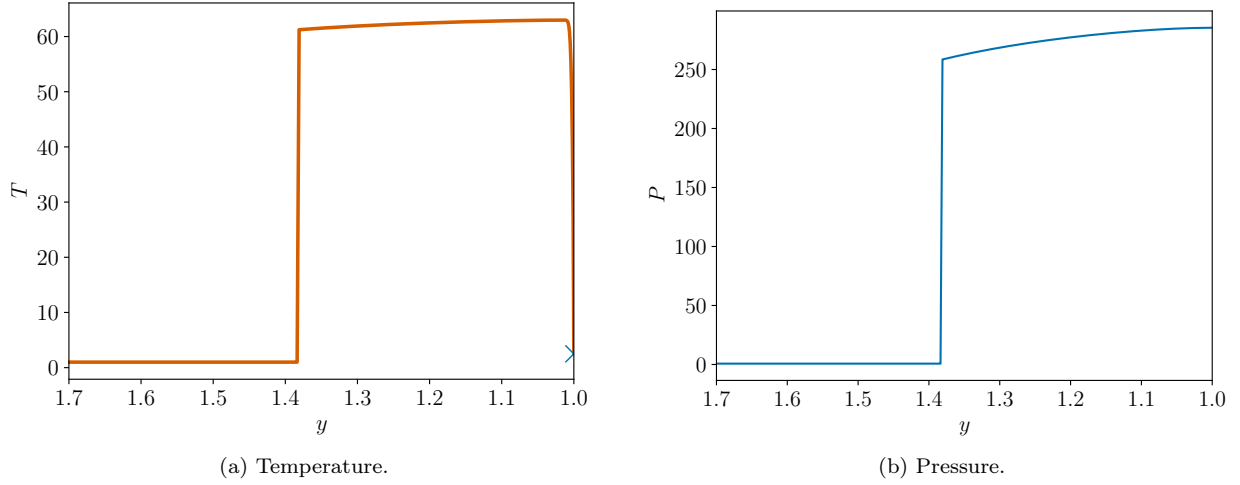


Figure 5.19: Stagnation-line profiles of temperature and pressure obtained with the MDG-ICE solution computed using 3024 $\mathcal{P}_5/\mathcal{P}_4$ subparametric triangle elements for three-dimensional Mach 17.6 flow over a cylinder at $Re = 376,930$. The stagnation point is located at $y = 1$. The exact stagnation-point temperature, $T = 2.5$, is marked with the symbol \times .

Figure 5.20 gives the surface pressure and heat flux evaluated at all degrees of freedom corresponding to Σ_h for the isoparametric MDG-ICE(\mathcal{P}_4) and subparametric MDG-ICE($\mathcal{P}_5/\mathcal{P}_4$) solutions. The pressure profiles agree very well. The heat flux near the stagnation point in the isoparametric MDG-ICE(\mathcal{P}_4) solution exhibits noticeable (though small compared to those observed in finite volume predictions [15, 14]) asymmetries that are largely eliminated in the subparametric MDG-ICE($\mathcal{P}_5/\mathcal{P}_4$) solution. Though very slight asymmetries are still present, the heat-flux profile is nevertheless highly symmetric. The stagnation-point Stanton number in the MDG-ICE($\mathcal{P}_5/\mathcal{P}_4$) solution is approximately 0.0077.

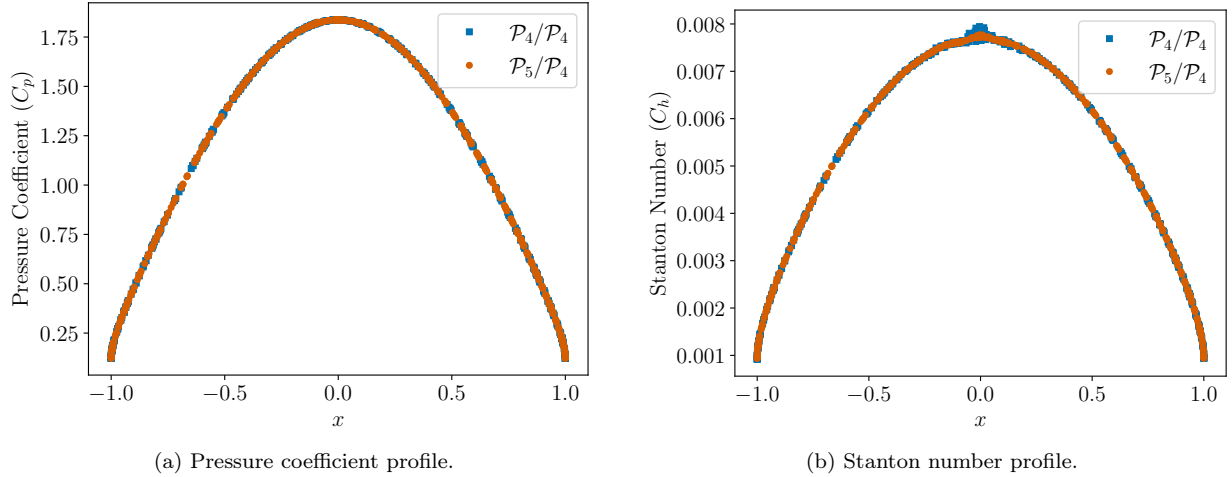


Figure 5.20: Surface profiles of pressure coefficient and Stanton number for the isoparametric MDG-ICE(\mathcal{P}_4) and subparametric MDG-ICE($\mathcal{P}_5/\mathcal{P}_4$) solutions to three-dimensional Mach 17.6 flow over a cylinder at $Re = 376,930$. Pressure and heat-flux values at all auxiliary-variable degrees of freedom along the cylinder wall are shown.

5.4. Mach 5 flow over three-dimensional sphere

In our final test case, we compute steady Mach 5 viscous flow over a hemisphere in three spatial dimensions. Only one quarter of the hemisphere, which is of unit radius, is considered in order to reduce

computational cost. The Reynolds number (based on the sphere radius) is 3.775×10^6 . The sphere boundary is an isothermal no-slip wall with temperature $T_{\text{wall}} = 1.308T_{\infty}$. These conditions are similar to those considered by Blottner [39] and in the 2022 High-Fidelity CFD Workshop [40, 41], except the Reynolds number here is four times higher. Freestream conditions are imposed at the inflow boundary, defined as a quarter hemisphere with radius 2.3 times larger than that of the spherical body. Extrapolation is applied at the outflow boundary. Despite the lower Mach number, the higher Reynolds number and inherently three-dimensional nature of the flow makes this problem more challenging than the previous test case.

Continuation in Reynolds number is employed. Figure 5.21 presents the initial 7650-cell tetrahedral grid and an isoparametric $\text{DG}(\mathcal{P}_2)$ solution at $\text{Ma} = 5, \text{Re} = 100$, which is used to initialize the MDG-ICE continuation with isoparametric \mathcal{P}_3 elements. The sphere surface and the $y = 0$ and $z = 0$ planes are displayed. Mesh imprinting along the sphere boundary and a highly diffused shock are observed in the DG solution. Given the cost of the LDLT linear solver, to maximize efficiency, the initial mesh is generated such that the azimuthal resolution is higher near the stagnation line than elsewhere. Furthermore, the wall-normal resolution is decreased near the inflow boundary. We also find that as the Reynolds number is increased, due to higher gradients at the shock than at the boundary layer, the solver tends to move cells from the near-wall region to the vicinity of the shock. To alleviate this loss of boundary-layer resolution, a very thin layer of cells is constructed adjacent to the wall. This issue can likely be resolved with localized artificial dissipation (to reduce gradients at the shock), a robust remeshing strategy, and/or local p -refinement, all of which will be pursued in the future. Nevertheless, we note that building an initial grid with additional resolution near the boundary surface is significantly simpler than constructing a grid with the required resolution in the wall-normal direction near the boundary surface while simultaneously aligning the grid interfaces with shocks, whose locations are generally unknown a priori.

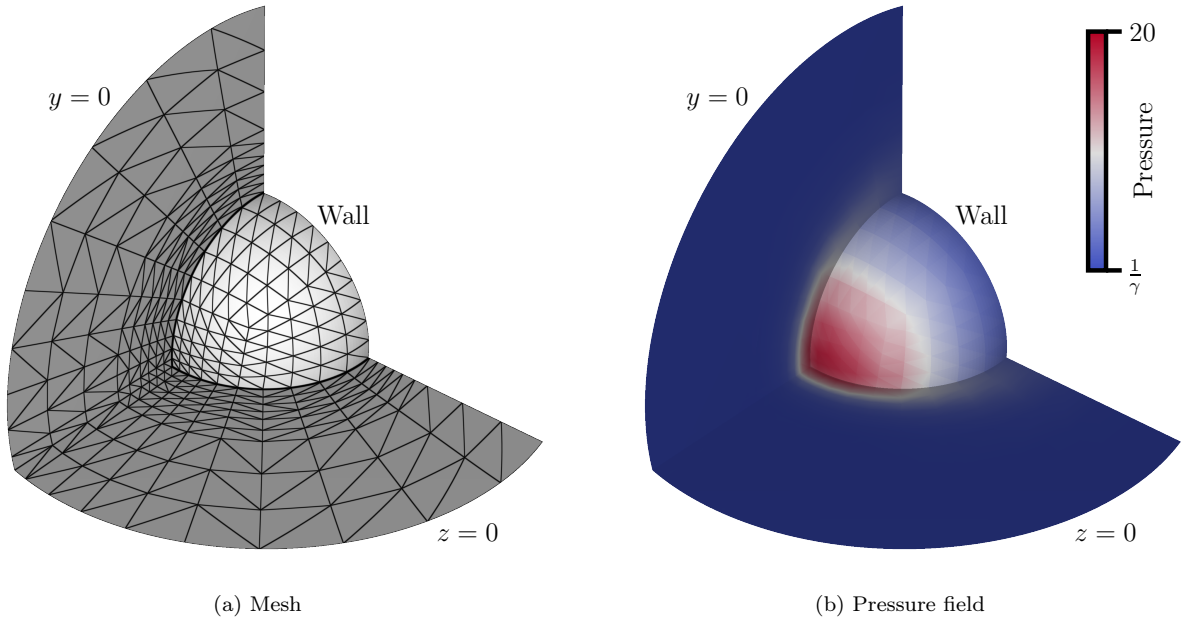


Figure 5.21: Isoparametric $\text{DG}(\mathcal{P}_2)$ solution at $\text{Ma} = 5, \text{Re} = 100$ on 7650 tetrahedral cells. This solution is used as the initial condition for the MDG-ICE continuation strategy. The sphere surface and the $y = 0$ and $z = 0$ planes are displayed.

Successive increases in the Reynolds number leads to the appearance of temperature undershoots that are especially difficult to dampen in this problem in the absence of artificial dissipation. To mitigate

these instabilities, we employ the least-squares MDG-ICE formulation with optimal test functions [3] based on the discontinuous Petrov-Galerkin methodology by Demkowicz and Gopalakrishnan [42, 43, 44]. This formulation is found to be significantly more robust (in terms of preventing spurious undershoots/overshoots in flow quantities) than the standard MDG-ICE formulation. The nonlinear-solver strategies described in Section 4 are incorporated in an analogous manner.

Figure 5.22 displays the final subparametric MDG-ICE($\mathcal{P}_5/\mathcal{P}_3$) solution at $\text{Ma} = 5, \text{Re} = 3.775 \times 10^6$. To reduce the number of unnecessary elements in the freestream region, we project the inflow boundary to a quarter hemisphere of radius 2.15. Cell collapses [23] are then performed to remove invalid cells, resulting in 7161 elements. The final grid is shown in Figure 5.22a. The surface mesh is noticeably coarse. The pressure field and surface heat-flux profile, presented in Figures 5.22b and 5.22c, respectively, are free from mesh imprinting and spurious oscillations. Figure 5.22d provides a zoomed-in view of the temperature field along the $z = 0$ plane. The temperature gradient in the boundary layer can be observed. The viscous shock resembles a true discontinuity, and the cells resolving the shock cannot be individually discerned. Nevertheless, grid validity is maintained. Note the closer proximity of the shock to the boundary layer than in the cylinder problem, despite a lower Mach number, which helps explain the aforementioned issue in which the solver moves grid points from the boundary layer to the shock.

The convergence history for the subparametric MDG-ICE($\mathcal{P}_5/\mathcal{P}_3$) solution is presented in Figure 5.23. The initial residual is already low since we restart from a subparametric MDG-ICE($\mathcal{P}_4/\mathcal{P}_3$) calculation. Figure 5.24 display profiles of temperature and pressure along the stagnation line. The stagnation point is located at $x = -1$. These results further exemplify the sharpness of the shock profile and the absence of spurious artifacts in the solution.

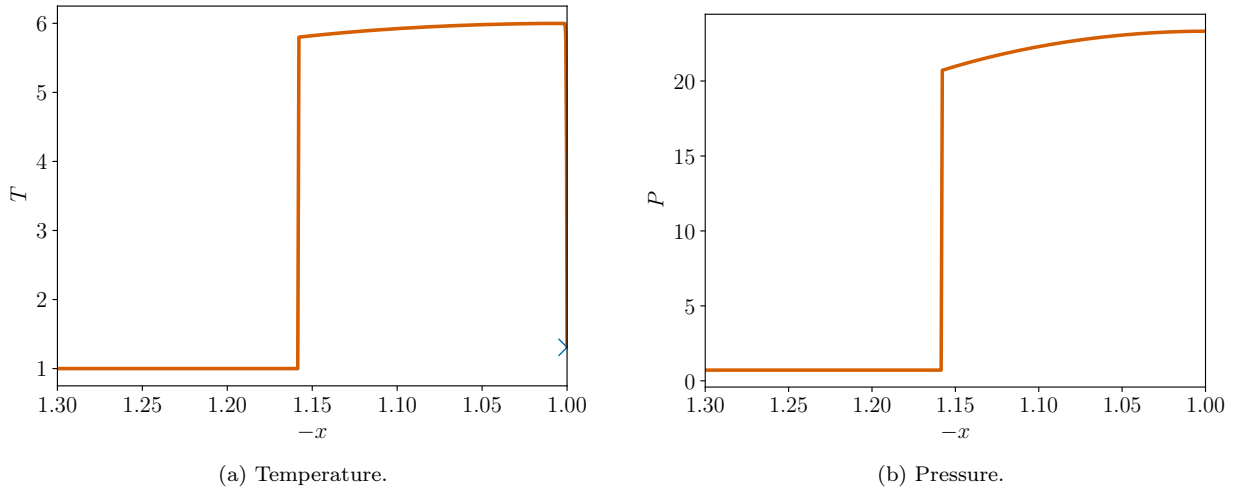


Figure 5.24: Stagnation-line profiles of temperature and pressure obtained with the MDG-ICE solution computed using 7161 $\mathcal{P}_5/\mathcal{P}_3$ subparametric triangle elements for three-dimensional Mach 5 flow over a sphere at $\text{Re} = 3.775 \times 10^6$. The stagnation point is located at $x = -1$. The exact stagnation-point temperature, $T = 1.308$, is marked with the symbol \times .

Figure 5.25 presents the streamwise variation of surface pressure and heat flux evaluated at all degrees of freedom corresponding to Σ_h for subparametric MDG-ICE($\mathcal{P}_4/\mathcal{P}_3$) and MDG-ICE($\mathcal{P}_5/\mathcal{P}_3$) solutions. The surface pressure is essentially perfectly symmetric. Noticeable asymmetries in the heat flux near the stagnation point for the MDG-ICE($\mathcal{P}_4/\mathcal{P}_3$) solution are observed. These asymmetries are significantly reduced in the MDG-ICE($\mathcal{P}_5/\mathcal{P}_3$) solution, resulting in a highly symmetric heat-flux profile. Note that potential interaction between the symmetry boundaries near the stagnation point may be a partial source of the small asymmetries. The stagnation-point Stanton number in the MDG-ICE($\mathcal{P}_5/\mathcal{P}_3$) solution is approximately 0.00167, which agrees well with the value of 0.00159 obtained using the correlation by Fay and Riddell [45]. These results demonstrate the ability of MDG-ICE, combined with the enhanced solver strategies intro-

duced in this work, to produce very accurate surface heating predictions even in the presence of considerable misalignment between the grid and the high-gradient features.

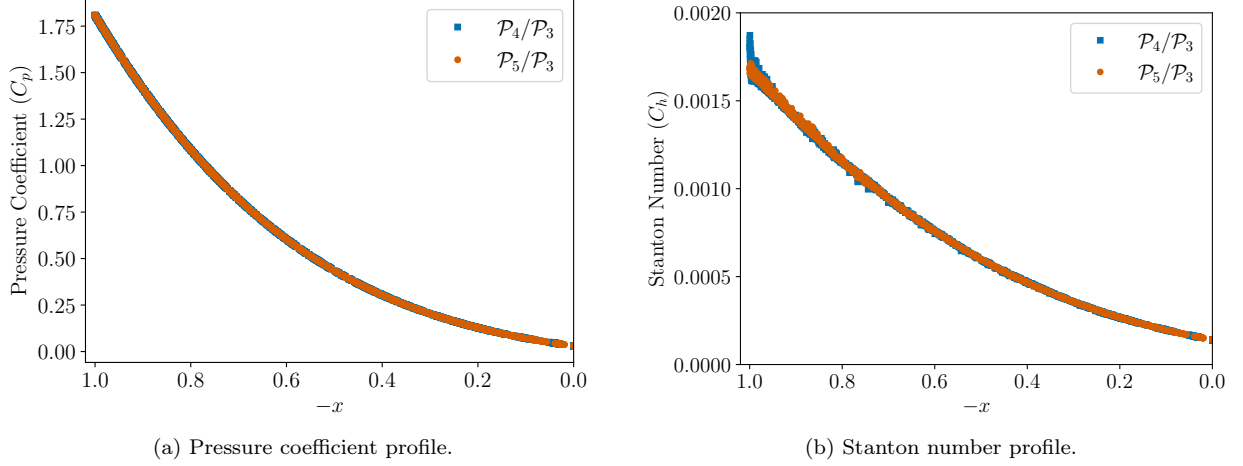


Figure 5.25: Streamwise variation of surface pressure and surface heat flux for the subparametric MDG-ICE($\mathcal{P}_5/\mathcal{P}_3$) solutions to three-dimensional Mach 5 flow over a sphere at $\text{Re} = 3.775 \times 10^6$. Pressure and heat-flux values at all auxiliary-variable degrees of freedom along the sphere wall are shown. The stagnation point is located at $x = -1$.

6. Conclusions and future work

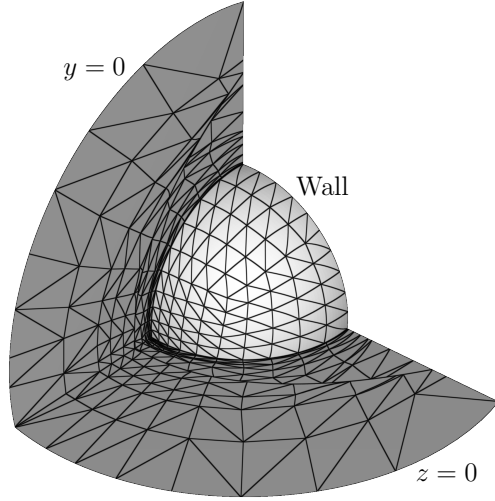
We introduced enhanced nonlinear solver strategies for the moving discontinuous Galerkin method with interface condition enforcement (MDG-ICE), which automatically fits discontinuous and high-gradient features without a priori information via curvilinear r -adaptivity in both space and time. Specifically, to overcome the major bottleneck of frequent cell degeneration, we incorporated additional regularization terms in the nonlinear least-squares solver, devised an anisotropic regularization based on the mesh-implied metric, and developed an adaptive elementwise regularization that locally increases the regularization parameters as needed to maintain grid validity. The proposed MDG-ICE formulation, without any explicit stabilization mechanisms, was applied to three test cases involving sharp yet smooth gradients: Burgers viscous shock formation in space-time, Mach 17.6 viscous flow over a circular half-cylinder in two and three dimensions, and Mach 5 flow over a three-dimensional sphere. We used simplicial grids in order to evaluate the ability of the developed MDG-ICE formulation to obtain symmetric surface heat-flux profiles in the presence of strong misalignment between the grid and the shock and boundary layer, which is considerably challenging for conventional numerical methods. Oscillation-free solutions and highly symmetric heating predictions were achieved.

Although the results presented in this work are very promising and demonstrate how MDG-ICE can significantly alleviate the burden of mesh generation on the user, additional advancements are needed in order to more fully realize its potential. Specifically, we plan to incorporate localized artificial dissipation (either only during intermediate iterations or in minimal amounts in the final solution), time marching via space-time MDG-ICE, local p -refinement, and improvements to the Levenberg-Marquardt method [28]. In addition, we will integrate metric-based mesh regeneration/adaptation strategies into the solver, potentially utilizing the mesh-implied metric naturally produced by an MDG-ICE solution, which should already yield small element length scales at high-gradient features. These developments will likely accelerate convergence, mitigate the need for continuation in Mach number and Reynolds number, and allow for even coarser initial grids. We will also explore treating strong viscous shocks as true discontinuities as an intrinsic feature of the solver (i.e., without the use of ad hoc strategies); layers of high-aspect-ratio cells would then no longer be required since discontinuous shocks can simply be fit along grid interfaces, as in the inviscid setting [1]. Finally, the efficiency of solving the linear system will be improved.

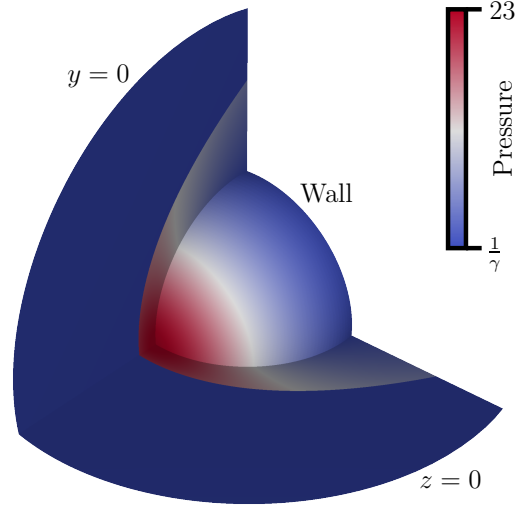
References

- [1] A. Corrigan, A. Kercher, D. Kessler, A moving discontinuous Galerkin finite element method for flows with interfaces, *International Journal for Numerical Methods in Fluids* 89 (9) (2019) 362–406. doi:10.1002/flid.4697.
- [2] A. Kercher, A. Corrigan, D. Kessler, The moving discontinuous Galerkin finite element method with interface condition enforcement for compressible viscous flows, *International Journal for Numerical Methods in Fluids* 93 (5) (2021) 1490–1519. doi:10.1002/flid.4939.
- [3] A. Kercher, A. Corrigan, A least-squares formulation of the moving discontinuous Galerkin finite element method with interface condition enforcement, *Computers & Mathematics with Applications* 95 (2021) 143–171. doi:10.1016/j.camwa.2020.09.012.
- [4] W. H. Reed, T. Hill, Triangular mesh methods for the neutron transport equation, Tech. rep., Los Alamos Scientific Lab., N. Mex.(USA) (1973).
- [5] B. Cockburn, G. Karniadakis, C.-W. Shu, The development of discontinuous Galerkin methods, in: *Discontinuous Galerkin Methods*, Springer, 2000, pp. 3–50.
- [6] A. Majda, Compressible fluid flow and systems of conservation laws in several space variables, Springer Science & Business Media, 2012. doi:10.1007/978-1-4612-1116-7.
- [7] E. Ching, Y. Lv, P. Gnoffo, M. Barnhardt, M. Ihme, Shock capturing for discontinuous Galerkin methods with application to predicting heat transfer in hypersonic flows, *Journal of Computational Physics* 376 (2018) 54–75. doi:10.1016/j.jcp.2018.09.016.
- [8] M. Zahr, P.-O. Persson, An optimization-based approach for high-order accurate discretization of conservation laws with discontinuous solutions, *Journal of Computational Physics* 365 (2018) 105–134. doi:10.1016/j.jcp.2018.03.029.
- [9] M. Zahr, A. Shi, P.-O. Persson, Implicit shock tracking using an optimization-based high-order discontinuous Galerkin method, *Journal of Computational Physics* 410 (2020) 109385. doi:10.1016/j.jcp.2020.109385.
- [10] A. Shi, P.-O. Persson, M. J. Zahr, Implicit shock tracking for unsteady flows by the method of lines, *Journal of Computational Physics* 454 (2022) 110906.
- [11] T. Huang, M. J. Zahr, A robust, high-order implicit shock tracking method for simulation of complex, high-speed flows, *Journal of Computational Physics* 454 (2022) 110981.
- [12] T. Huang, C. J. Naudet, M. J. Zahr, High-order implicit shock tracking boundary conditions for flows with parametrized shocks, *Journal of Computational Physics* (2023) 112517.
- [13] H. Luo, G. Absillis, R. Nourgaliev, A moving discontinuous Galerkin finite element method with interface condition enforcement for compressible flows, *Journal of Computational Physics* 445 (2021) 110618.
- [14] I. Nompelis, T. Drayna, G. Candler, Development of a hybrid unstructured implicit solver for the simulation of reacting flows over complex geometries, in: *34th AIAA Fluid Dynamics Conference and Exhibit*, 2004, p. 2227, AIAA-2004-2227. doi:10.2514/6.2004-2227.
- [15] P. Gnoffo, J. White, Computational aerothermodynamic simulation issues on unstructured grids, in: *37th AIAA Thermophysics Conference*, 2004, p. 2371, AIAA-2004-2371. doi:10.2514/6.2004-2371.
- [16] K. J. Fidkowski, A simplex cut-cell adaptive method for high-order discretizations of the compressible Navier-Stokes equations, Ph.D. thesis, Massachusetts Institute of Technology (2007).
- [17] M. Ceze, K. J. Fidkowski, Constrained pseudo-transient continuation, *International Journal for Numerical Methods in Engineering* 102 (11) (2015) 1683–1703.
- [18] K. Levenberg, A method for the solution of certain non-linear problems in least squares, *Quarterly of applied mathematics* 2 (2) (1944) 164–168. doi:10.1090/qam/10666.
- [19] D. Marquardt, An algorithm for least-squares estimation of nonlinear parameters, *Journal of the society for Industrial and Applied Mathematics* 11 (2) (1963) 431–441. doi:10.1137/0111030.
- [20] E. Ching, M. Ihme, Efficient projection kernels for discontinuous Galerkin simulations of disperse multiphase flows on arbitrary curved elements, *Journal of Computational Physics* 435 (2021) 110266. doi:10.1016/j.jcp.2021.110266.
- [21] T. Toulorge, C. Geuzaine, J.-F. Remacle, J. Lambrechts, Robust untangling of curvilinear meshes, *Journal of Computational Physics* 254 (2013) 8–26.
- [22] F. Alauzet, A changing-topology moving mesh technique for large displacements, *Engineering with Computers* 30 (2) (2014) 175–200.
- [23] R. Löhner, *Applied CFD Techniques*, J. Wiley & Sons, 2008.
- [24] Z. Q. Xie, R. Sevilla, O. Hassan, K. Morgan, The generation of arbitrary order curved meshes for 3D finite element analysis, *Computational Mechanics* 51 (2013) 361–374.
- [25] D. Moxey, D. Ekelschot, Ü. Keskin, S. J. Sherwin, J. Peiró, High-order curvilinear meshing using a thermo-elastic analogy, *Computer-Aided Design* 72 (2016) 130–139.
- [26] J. Marcon, A. Garai, M. Denison, S. M. Murman, An adjoint elasticity solver for high-order mesh deformation, in: *AIAA Scitech 2021 Forum*, 2021, p. 1238.
- [27] A. Gargallo-Peiró, X. Roca, J. Peraire, J. Sarrate, Distortion and quality measures for validating and generating high-order tetrahedral meshes, *Engineering with Computers* 31 (3) (2015) 423–437.
- [28] M. K. Transtrum, J. P. Sethna, Improvements to the Levenberg-Marquardt algorithm for nonlinear least-squares minimization, arXiv preprint arXiv:1201.5885 (2012).
- [29] P. Amestoy, I. S. Duff, J. Koster, J.-Y. L’Excellent, A fully asynchronous multifrontal solver using distributed dynamic scheduling, *SIAM Journal on Matrix Analysis and Applications* 23 (1) (2001) 15–41.
- [30] P. Amestoy, A. Buttari, J.-Y. L’Excellent, T. Mary, Performance and scalability of the block low-rank multifrontal factorization on multicore architectures, *ACM Transactions on Mathematical Software* 45 (2019) 2:1–2:26.

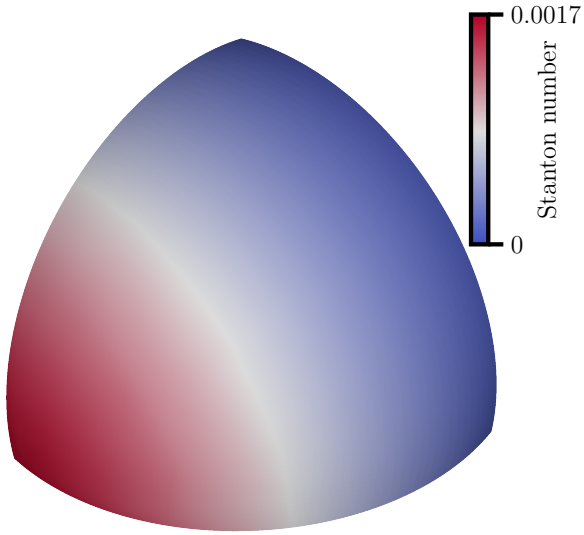
- [31] S. Balay, W. D. Gropp, L. C. McInnes, B. F. Smith, Efficient management of parallelism in object oriented numerical software libraries, in: E. Arge, A. M. Bruaset, H. P. Langtangen (Eds.), *Modern Software Tools in Scientific Computing*, Birkhäuser Press, 1997, pp. 163–202.
- [32] S. Balay, S. Abhyankar, M. F. Adams, S. Benson, J. Brown, P. Brune, K. Buschelman, E. Constantinescu, L. Dalcin, A. Dener, V. Eijkhout, J. Faibussowitsch, W. D. Gropp, V. Hapla, T. Isaac, P. Jolivet, D. Karpeev, D. Kaushik, M. G. Knepley, F. Kong, S. Kruger, D. A. May, L. C. McInnes, R. T. Mills, L. Mitchell, T. Munson, J. E. Roman, K. Rupp, P. Sanan, J. Sarich, B. F. Smith, S. Zampini, H. Zhang, H. Zhang, J. Zhang, PETSc/TAO users manual, Tech. Rep. ANL-21/39 - Revision 3.20, Argonne National Laboratory (2023). doi:10.2172/1968587.
- [33] G. Barter, D. Darmofal, Shock capturing with PDE-based artificial viscosity for DGFEM: Part I. formulation, *Journal of Computational Physics* 229 (5) (2010) 1810–1827. doi:10.1016/j.jcp.2009.11.010.
- [34] R. F. Johnson, A. D. Kercher, A conservative discontinuous Galerkin discretization for the chemically reacting Navier-Stokes equations, *Journal of Computational Physics* 423 (2020) 109826. doi:10.1016/j.jcp.2020.109826.
- [35] K. Kitamura, E. Shima, Towards shock-stable and accurate hypersonic heating computations: A new pressure flux for AUSM-family schemes, *Journal of Computational Physics* 245 (2013) 62–83.
- [36] Y. Lv, M. Ihme, Entropy-bounded discontinuous Galerkin scheme for Euler equations, *Journal of Computational Physics* 295 (2015) 715–739.
- [37] Y. Jiang, H. Liu, Invariant-region-preserving DG methods for multi-dimensional hyperbolic conservation law systems, with an application to compressible Euler equations, *Journal of Computational Physics* 373 (2018) 385–409.
- [38] E. J. Ching, R. F. Johnson, A. D. Kercher, Positivity-preserving and entropy-bounded discontinuous Galerkin method for the chemically reacting, compressible Euler equations. Part I: The one-dimensional case, arXiv preprint arXiv:2211.16254 <https://arxiv.org/abs/2211.16254> (2022).
- [39] F. Blottner, Accurate Navier-Stokes results for the hypersonic flow over a spherical nosetip, *Journal of spacecraft and Rockets* 27 (2) (1990) 113–122. doi:10.2514/3.26115.
- [40] T. Fisher, High fidelity CFD workshop 2021: High speed steady advanced case: Blottner sphere, NASA Langley Research Center Turbulence Modeling Resource https://turbmodels.larc.nasa.gov/highfidelitycfdf_{workshop2022}.html (2021).
- [41] A. R. Murphy, R. K. Agarwal, Computational analysis of laminar steady hypersonic flow past Blottner sphere using ANSYS Fluent, in: *AIAA AVIATION 2023 Forum*, 2023, p. 3847, AIAA-2023-3847.
- [42] L. Demkowicz, J. Gopalakrishnan, A class of discontinuous Petrov–Galerkin methods. Part I: The transport equation, *Computer Methods in Applied Mechanics and Engineering* 199 (23–24) (2010) 1558–1572. doi:10.1016/j.cma.2010.01.003.
- [43] L. Demkowicz, J. Gopalakrishnan, A class of discontinuous Petrov–Galerkin methods. II. Optimal test functions, *Numerical Methods for Partial Differential Equations* 27 (1) (2011) 70–105. doi:10.1002/num.20640.
- [44] L. Demkowicz, J. Gopalakrishnan, Discontinuous Petrov-Galerkin (DPG) method, Tech. Rep. 15-20, ICES, retrieved from <https://www.odn.utexas.edu/media/reports/2015/1520.pdf> (October 2015).
- [45] J. A. Fay, F. Riddell, Theory of stagnation point heat transfer in dissociated air, *Journal of the Aerospace Sciences* 25 (2) (1958) 73–85.



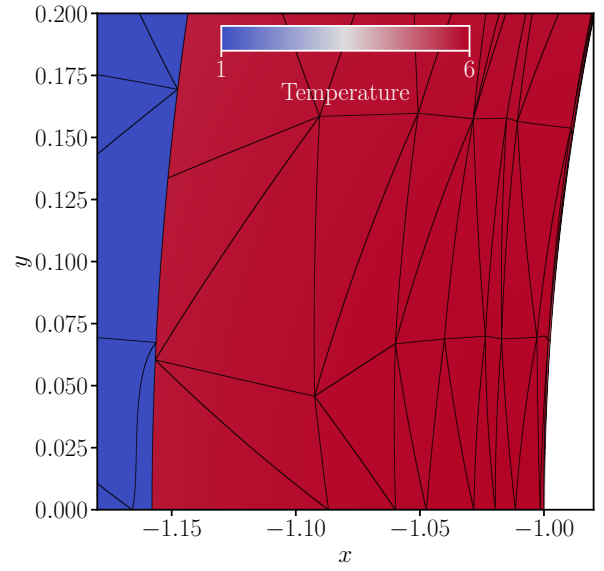
(a) Mesh.



(b) Pressure field.



(c) Surface heat flux.



(d) Zoomed-in view of temperature profile along $z = 0$ plane.

Figure 5.22: Final grid and pressure field for a subparametric MDG-ICE($\mathcal{P}_5/\mathcal{P}_3$) solution to hypersonic flow over a sphere at $\text{Ma} = 5$, $\text{Re} = 3.775 \times 10^6$. In Figures 5.22a and 5.22b, the $y = 0$ and $z = 0$ planes and the sphere wall are displayed.

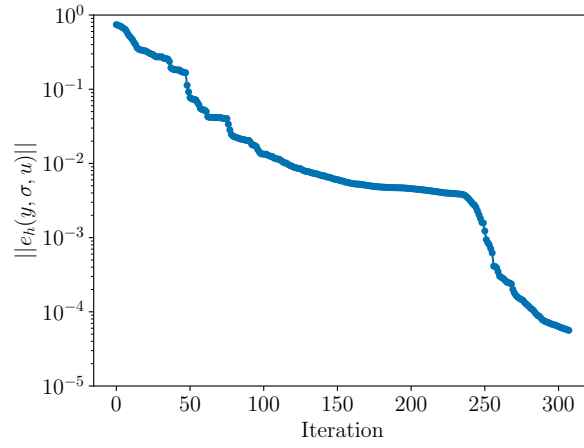


Figure 5.23: Nonlinear convergence history for the subparametric MDG-ICE($\mathcal{P}_5/\mathcal{P}_3$) solution to Mach 5 flow over a sphere.